

The Milky Way as a Star Formation Engine

¹Sergio Molinari, ²John Bally, ³Simon Glover, ⁴Toby Moore, ⁵Alberto Noriega-Crespo, ⁶René Plume, ^{7,8,9}Leonardo Testi, ¹⁰Enrique Vázquez-Semadeni, ¹¹Annie Zavagno, ¹²Jean-Philippe Bernard, ¹³Peter Martín

1. INAF-Istituto di Astrofisica e Planetologia Spaziali, Via Fosso del Cavaliere 100, I-00133 Rome, Italy, **2.** Center for Astrophysics and Space Astronomy, UCB 389, University of Colorado at Boulder, Boulder CO 80389, USA **3.** Universität Heidelberg, Zentrum für Astronomie, Institut für Theoretische Astrophysik, Albert-Ueberle-Str. 2, 69120 Heidelberg, Germany, **4.** Astrophysics Research Institute, Liverpool John Moores University, Twelve Quays House, Egerton Wharf, Birkenhead CH41 1LD, UK, **5.** Space Telescope Science Institute, 3700 San Martin Drive, Baltimore, MD 21218, USA **6.** University of Calgary, Dept. of Physics & Astronomy, 2500 University Dr. NW, Calgary, AB, T2N1N4, Canada, **7.** ESO, Karl Schwarzschild str. 2, D-85748 Garching, Germany, **8.** INAF-Osservatorio Astrofisico di Arcetri, Largo E. Fermi 5, I-50125 Firenze, Italy **9.** Excellence Cluster Universe, Boltzmannstr. 2, D-85748 Garching, Germany **10.** Centro de Radioastronomía y Astrofísica, Universidad Nacional Autónoma de México, Campus Morelia, Apdo. Postal 3-72, Morelia, 58089, México, **11.** Aix Marseille Université, CNRS, LAM (Laboratoire d'Astrophysique de Marseille) UMR 7326, 13388, Marseille, France **12.** Institut de Recherche en Astrophysique et Planétologie, 9, av. du Colonel-Roche - BP 44 346, 31028 Toulouse Cedex 4 France, **13.** Canadian Institute for Theoretical Astrophysics, University of Toronto, 60 St. George Street, Toronto, ON M5S 3H8, Canada

The cycling of material from the interstellar medium (ISM) into stars and the return of stellar ejecta into the ISM is the engine that drives the *galactic ecology* in normal spirals. This ecology is a cornerstone in the formation and evolution of galaxies through cosmic time. There remain major observational and theoretical challenges in determining the processes responsible for converting the low-density, diffuse components of the ISM into dense molecular clouds, forming dense filaments and clumps, fragmenting them into stars, expanding OB associations, and bound clusters, and characterizing the feedback that limits the rate and efficiency of star formation. This formidable task can be attacked effectively for the first time thanks to the synergistic combination of new global-scale surveys of the Milky Way from infrared to radio wavelengths, offering the possibility of bridging the gap between local and extragalactic star formation studies.

The Herschel Hi-GAL survey, with its five-band 70–500 μm full Galactic Plane mapping at 6–36'' resolution, is the keystone of a set of continuum surveys that include GLIMPSE(360)+MIPSGAL@Spitzer, WISE and MSX, ATLASGAL@APEX, BGPS@CSO, and CORNISH@VLA. This suite enables us to measure the Galactic distribution and physical properties of dust on all scales and in all components of the ISM from diffuse clouds to filamentary complexes and hundreds of thousands of dense clumps. A complementary suite of spectroscopic surveys in various atomic and molecular tracers is providing the chemical fingerprinting of dense clumps and filaments, as well as essential kinematic information to derive distances and thus transform panoramic data into a 3D representation.

The latest results emerging from these Galaxy-scale surveys are reviewed. New insights into cloud formation and evolution, filaments and their relationship to channeling gas onto gravitationally-bound clumps, the properties of these clumps, density thresholds for gravitational collapse, and star and cluster formation rates are discussed.

1. Introduction

Phase changes in the Galactic ISM are to a large extent controlled by the formation of massive stars. The cycling of the ISM from mostly neutral atomic (H I) clouds into molecular (H₂) clouds, traced by low-excitation species such as OH and CO, leads to the formation of dense, self-gravitating clumps and cores traced by high-density species such as NH₃, CS, HCN, HCO⁺, and N₂H⁺, and by other even higher dipole moment molecules in regions where stars form.

Dust continuum emission in the mid-IR, far-IR, submillimeter (submm), and millimeter ranges of the spectrum reveal progressively cooler and higher column density

dust associated with all phases of the ISM, and with the high-density material in protostellar envelopes and disks. Dust extinction measurements in the UV, visual, near-IR, and mid-IR enable detection of progressively higher column densities of dust located in front of background stellar and diffuse emission sources.

Feedback from young stars limits the rate and efficiency of star formation by generating turbulence and disrupting the parent clouds. In giant molecular clouds (GMCs) feedback, usually dominated by the most massive young stellar objects (YSOs), tends to disrupt the parent cloud by the time 2–20% of its mass has formed stars. Ionization and shocks produced by massive stars, associations, and clusters con-

vert the remaining gas into the 10^4 – 10^8 K photoionized and shock-heated phases of the ISM – HII regions traced by H and He recombination lines and free-free emission, hot superbubbles traced by X-ray emission, and 0.1 to 1 kpc-scale supershells – that eventually cool, condense, and reform the cool ~ 20 to 10^4 K HI phase. Compression by shocks and gravity leads to the formation of new GMCs.

In the Solar vicinity, atoms cycle through this loop on a time scale of 50–100 My. A mean star formation efficiency (SFE) of 5% per GMC implies that atoms on average pass through this loop about 20 times before being incorporated into a star. This *galactic ecology* is modulated by large-scale processes such as spiral arms and the central bar of the Milky Way. While star formation depletes the ISM at a rate of $\sim 2 M_{\odot} \text{ y}^{-1}$, infall of gas from the Local Group supplements it at a highly uncertain rate of 0.1 to $1 M_{\odot} \text{ y}^{-1}$. The balance between star formation, which sequesters matter for the main-sequence lifetime of stars, and recycling from stellar winds and dying stars, supplemented by infall from the Local Group, determines the time scale on which the Galactic ISM is depleted. Large-scale Galactic plane surveys of the last decade provide the data required to flesh out the details of this *galactic ecology*.

The Milky Way, a mildly-barred, gas-rich spiral galaxy, supports the most active star formation in the Local Group. The Galactic disk contains about 1 – $3 \times 10^9 M_{\odot}$ of H_2 and about 2 – $6 \times 10^9 M_{\odot}$ of HI (Combes, 1991; Kalberla and Kerp, 2009). The molecular disk becomes prominent from Galactocentric radius $R_{gal} \sim 3$ kpc, beyond the central bar, with surface density peaking at about $R_{gal} \sim 4$ – 6 kpc (often referred to as the *Molecular Ring*). It declines exponentially toward larger radii but can be traced well beyond $R_{gal} \sim 10$ kpc. The HI disk extends to beyond $R_{gal} \sim 20$ kpc. The disk ISM is dominated by a four-arm spiral pattern consisting of two major and two minor spiral arms and a variety of inter-arm spurs. The Sun is currently located in an inter-arm region between the Sagittarius and Perseus spiral arms, near a spur which extends from a distance of several kpc in the direction of Cygnus to at least 1 kpc beyond Orion in the opposite direction (Xu et al., 2013). In molecular tracers such as CO, the arm–inter-arm contrast in the Molecular Ring is around 3:1, but in the outer Galaxy beyond the Solar circle at $R_{gal} \approx 8.5$ kpc the contrast is much higher, approaching a value of 40:1 toward the Perseus arm.

Although Galactic rotation is well described by circular motions with orbit speeds ranging from 200 to 250 km s^{-1} from $R_{gal} \sim 1$ kpc to beyond 20 kpc, substantial radial motions are seen in gas tracers toward the Galactic Center and Anti-center. The line of sight toward the Galactic Center shows three clearly-defined spiral arms, distinguished by their negative radial velocities with respect to the local standard of rest (LSR; defined by the mean motion of stars in the Solar vicinity). The innermost is the so-called 3-kpc arm in the Molecular Ring ($V_{LSR} \approx -60 \text{ km s}^{-1}$), next is the Scutum arm ($V_{LSR} \approx -35 \text{ km s}^{-1}$), and then closest (~ 2 kpc) is the Sagittarius arm ($V_{LSR} \approx -15 \text{ km s}^{-1}$). Radial streaming motions of order 10 to 30 km s^{-1} are also

seen toward the Perseus arm and the far outer arm beyond that. These motions might reflect the gravitational potential well depth of the spiral arms.

The inner edge of the Molecular Ring at $R_{gal} \sim 3$ kpc lies near the outer radius of the Galactic bulge and bar. The central 3-kpc region of the Galaxy is dominated by the stellar bar whose major axis is inclined by 20° to 40° with respect to our line of sight (Binney et al., 1991; Morris and Serabyn, 1996). Within 0.5 kpc of the nucleus lies the Central Molecular Zone (CMZ) containing $\sim 10\%$ of the molecular gas in the Galaxy. The CMZ clouds are one to two orders of magnitude denser than GMCs in the Molecular Ring, and an order of magnitude more turbulent.

2. Physical Properties of the Milky Way ISM from Dust and Gas Tracers

With the advent of photography and multi-color photometry in the late 1800s and early 1900s the presence of interstellar dust was recognized by its extinction and reddening effect on the light from distant stars. Evidence for interstellar gas followed in the 1930s with the detection of narrow absorption lines of sodium and potassium and a few simple molecules such as CH and CH^+ . The discovery of the 21 cm line of HI in the 1940s led to the first all-sky surveys of the ISM and the recognition that the Galaxy contains more than $10^9 M_{\odot}$ of gas. The detection of absorption and thermal emission from OH, NH_3 , CO, and many other molecules in the 1960s and 1970s led to the discovery of molecular clouds and the recognition that GMCs were the birth sites of stars.

The last 30 years have seen an impressive set of infrared, millimeter, and radio surveys both in spectroscopy and in continuum bands that have covered the Galactic Plane. Table 1 gives a representative list. These have increased exponentially the amount of information available but at the same time have exposed the complexity of the puzzle of the *galactic ecology*.

2.1. Spectral Line Surveys

Detector technology has to a large extent dictated the development of Galactic plane surveys. From the late 1970s until the late 1990s, heterodyne receivers dominated, with a number of evermore detailed spectral line surveys of the entire sky in HI, portions of the Galactic plane in CO, and selected regions such as Orion, Sgr B2, and other star forming complexes as well as a few post-main sequence stars in a range of other molecular species.

Since the early 1970s, CO emission has been the most commonly used tracer of molecular gas in the Galaxy. The CO molecule is the most abundant species in molecular gas next to H_2 and He. Its small (~ 0.1 Debye) dipole moment results in bright CO emission widespread along the Galactic plane. Its large abundance ($\sim 10^{-4}$ times that of H_2), high opacity, and consequent radiative trapping enables CO to trace molecular gas at H_2 densities above $\sim 10^2 \text{ cm}^{-3}$. The first comprehensive survey in the CO $J = 1 - 0$ line

Table 1: List of most representative surveys covering the Galactic Plane

Surveys facilities	λ or lines	Surveys notes
Ground-based		
Columbia/CfA	CO, ^{13}CO	9 - 25' resolution (<i>Dame et al.</i> , 2001)
DRAO/ATCA/VLA	HI-21 cm OH/H α -RRL/1-2GHz cont. 5GHz cont.	IGPS: unbiased HI-21cm $255^\circ \leq l \leq 357^\circ$ and $18^\circ \leq l \leq 147^\circ$ (<i>McClure-Griffiths et al.</i> , 2001; <i>Gibson et al.</i> , 2000; <i>Stil et al.</i> , 2006) + THOR: unbiased HI-21cm/OH/H α -RRLs/1-2GHz cont. $15^\circ \leq l \leq 67^\circ$ (Beuther et al. in prep.)+ CORNISH: 5GHz continuum $10^\circ \leq l \leq 65^\circ$ (<i>Hoare et al.</i> , 2012) 55'' resolution. Galactic Ring Survey (<i>Jackson et al.</i> , 2006)
FCRAO 14 m	CO, ^{13}CO	+ Outer Galaxy Survey (<i>Heyer et al.</i> , 1998)
Mopra 22 m	CO, ^{13}CO , N $_2\text{H}^+$, (NH $_3$ + H $_2\text{O}$) maser, HCO $^+$ /H $^{13}\text{CO}^+$ + others	HOPS: (<i>Walsh et al.</i> , 2011; <i>Purcell et al.</i> , 2012), MALT90: ~ 2000 clumps $20^\circ \geq l \geq -60^\circ$ (<i>Foster et al.</i> , 2013), Southern GPS CO: unbiased $305^\circ \leq l \leq 345^\circ$ (<i>Burton et al.</i> , 2013), ThrUMMS: unbiased $300^\circ \leq l \leq 358^\circ$ (<i>Barnes et al.</i> , 2013), CMZ: (<i>Jones et al.</i> , 2012, 2013)
Parkes	CH $_3\text{OH}$ maser	Methanol MultiBeam Survey (<i>Green et al.</i> , 2009)
NANTEN/ NAN-TEN2	CO, ^{13}CO , C ^{18}O	NGPS: unbiased, $200^\circ \leq l \leq 60^\circ$ (<i>Mizuno and Fukui</i> , 2004)
CSO 10 m	1.3 mm continuum	+ NASCO: unbiased in progress, $160^\circ \leq l \leq 80^\circ$ Bolocam Galactic Plane Survey (BGPS), 33'' (<i>Aguirre et al.</i> , 2011)
APEX 12 m	870 μm continuum	ATLASGAL, $60^\circ \geq l \geq -80^\circ$ (<i>Schuller et al.</i> , 2009)
Space-borne		
IRAS	12, 25, 60 and 100 μm cont.	3-5', 96% of the sky
MSX	8.3, 12.1, 14.7, 21.3 μm cont.	Full Galactic Plane (<i>Price et al.</i> , 2001)
WISE	3.4, 4.6, 11, 22 μm continuum	All-sky (<i>Wright et al.</i> , 2010)
Akari	65, 90, 140, 160 μm continuum	All-sky (<i>Ishihara et al.</i> , 2010)
Spitzer	3.6, 4.5, 6, 8, 24 μm continuum	GLIMPSE+GLIMPSE360: Full Galactic Plane (<i>Benjamin et al.</i> , 2003), (<i>Benjamin and GLIMPSE360 Team</i> , 2013) + MIPS GAL, $63^\circ \geq l \geq -62^\circ$ (<i>Carey et al.</i> , 2009)
Planck	350, 550, 850, 1382, 2098, 3000, 4285, 6820, 10^4 μm cont.	All-sky, resolution $\geq 5'$ (<i>Planck Collaboration et al.</i> , 2013a)
Herschel	70, 160, 250, 350, 500 μm cont.	Hi-GAL: Full Galactic Plane (<i>Molinari et al.</i> , 2010a)

(*Dame et al.*, 1987) covered the Galactic plane over a latitude range of $10^\circ - 20^\circ$ with a grid resolution of 0.5° , and parts of Galactic plane with a resolution of $9'$, revealing the large-scale spatial and velocity distribution of CO-emitting molecular gas. *Dame et al.* (2001) combined spectra from 31 sub-surveys to cover $4^\circ - 10^\circ$ in latitude with $9'$ to $15'$ angular resolution. The first all-sky image of CO emission was produced from Planck data through careful analysis detector by detector of Planck HFI continuum images (*Planck Collaboration et al.*, 2013b). Velocity-integrated maps of the three lowest rotational transitions of CO were produced at $\sim 5'$ resolution. In the regions of overlap, the agreement between the Dame et al. and the Planck products is excellent. The Planck CO images reveal many new high-latitude CO-emitting clouds.

Higher angular resolution ($< \text{few arcminute}$) CO surveys cover selected portions of the Galactic Plane. The Five College Radio Astronomy Observatory (FCRAO) 14 m telescope surveyed the Northern Galactic plane with a resolution of $\sim 45''$ (*Heyer et al.*, 1998; *Roman-Duval et al.*, 2010). Data covering the remaining portions of the

Northern Galactic plane were obtained before FCRAO was closed, but have not yet been published. Selected regions of the Southern sky have been obtained with the NANTEN2, ASTE, APEX, and Mopra telescopes. Although CO is an excellent tracer of H $_2$, most of the gas traced by this low-excitation species is not directly associated with star formation.

Detailed studies of selected nearby molecular clouds such as those in Taurus, Ophiuchus, Perseus, and Orion, as well as of clouds in more distant portions of the Galactic plane, demonstrated that high-dipole moment (~ 2 to 4 Debye) species such as NH $_3$, CS, HCN, HCO $^+$, and N $_2\text{H}^+$ are more closely associated with dense, self-gravitating clumps and cores associated with the formation of clusters and individual stars. Recently, the Mopra telescope surveyed the Southern Milky Way in the 1.3 cm NH $_3$ and H $_2\text{O}$ maser lines (HOPS; *Walsh et al.* 2011). Mopra is also conducting surveys of dense gas tracers around 3 mm (MALT90; *Foster et al.* 2011, 2013), CH, and CO isotopologues (CHaMP; *Barnes et al.* 2011).

2.2. Continuum Surveys

The IRAS survey in the mid-1990s provided the first far-IR all-sky survey in the dust continuum. The development of focal plane arrays in the IR to far-IR wavelength region and submm bolometer arrays in the late 1990s led to a series of surveys including ISO, MSX, and COBE from space. The last decade has seen a number of large continuum surveys with Spitzer, AKARI, WISE, and, most recently, Herschel and Planck. The 12 m APEX telescope was used for the ATLASGAL survey of the Southern Galactic plane at $870\ \mu\text{m}$ (Schuller *et al.*, 2009). The 10 m CSO was used to obtain the 1.1 mm Bolocam Galactic Plane Survey (BGPS) of the Northern Galactic plane at $1300\ \mu\text{m}$ with a $33''$ beam (Aguirre *et al.*, 2011). The 15 m JCMT is being used for 850 and $450\ \mu\text{m}$ SCUBA2 surveys of the Galactic plane and several nearby Gould Belt clouds.

A major breakthrough in the study of massive star and cluster formation was the discovery of infrared dark clouds (IRDCs), which trace the highest column density clumps and cores in GMCs. Unbiased extractions of IRDCs from the MSX maps produced catalogs of several thousand clouds (Simon *et al.*, 2006). Variations in the mid-IR background, however, can mimic an IRDC without dense and cold intervening material. When a more refined approach was used to extract IRDCs from the higher quality Spitzer/IRAC images of the GLIMPSE survey (Benjamin *et al.*, 2003), Peretto and Fuller (2009) found twice as many clouds as Simon *et al.*, yet did not confirm many of Simon *et al.*'s IRDCs. It has been suggested that IRDCs are the high-mass analogues of low-mass prestellar cores. Early radio spectroscopic follow-up (e.g., Pillai *et al.*, 2006) suggested that star formation in IRDCs is ongoing. Peretto and Fuller (2009) showed that as many as 70% of their IRDCs were indeed associated with a $24\text{-}\mu\text{m}$ compact source from the Spitzer/MIPSGAL Survey (Carey *et al.*, 2009), again indicating ongoing star formation.

Dust continuum emission at far-IR, submm, and mm wavelengths provides a robust tracer of the dust column density and mean grain temperature along the line of sight, independent of the phase of the associated ISM. Surveys with Spitzer and WISE have mapped most of the Galactic plane at 3.6, 4.5, 6, 8, and $24\ \mu\text{m}$ with resolutions of a few to $10''$. The Herschel Space Observatory Galactic Plane Survey (Hi-GAL) and its successor extensions (Molinari *et al.*, 2010b) have mapped the entire Galactic plane in five bands at 70, 160, 250, 350, and $500\ \mu\text{m}$ with angular resolutions of about $6''$ to $36''$.

Distances must be determined to extract physical quantities from continuum data. Some dust continuum morphological features are associated with objects for which distances estimates exist. However, for the majority of continuum sources there are no such associations. Continuum surveys of the Galactic plane must be combined with complementary heterodyne surveys that provide measurements of the radial velocity of gas associated with dust continuum emission or absorption features. Most current distance-

determination methods rely on kinematic distances deduced from an axisymmetric Galactic rotation model combined with a variety of methods to resolve the kinematic distance ambiguity (KDA) for objects located within the Solar circle. However, systematic streaming motions and local peculiar velocities limit the precision of such distance estimates (Xu *et al.*, 2013).

Radial velocity measurements can be used to associate clumps and features for which there are no direct distance measurements with sources for which distance estimates exist. The Hi-GAL group working on distances (Russeil *et al.*, 2011) used the radial velocities of dust clumps and linked them to nearby sources (HII regions, stellar groups, or star forming regions) for which reliable distance estimates exist. This “bootstrapping” approach, together with the use of near-IR extinction mapping information to help resolve the KDA, has provided approximate distance estimates for tens of thousands of Hi-GAL sources (Elia *et al.*, 2014).

The key challenge for kinematic distance estimates is resolution of the KDA. Distance from the Galactic mid-plane, the presence of an associated IRDC, a 21 cm “HI narrow self-absorption” (HINSA) feature at the LSR velocity of the dust clump (produced by cold atomic hydrogen in and around the molecular cloud), and the density of foreground stars can be used to resolve the KDA. Association with a high-contrast IRDC, the presence of HINSA, significant displacement from the Galactic mid-plane, and a low density of foreground stars in the near-IR favor placement at the near kinematic distance. Absence of an associated IRDC and HINSA (because the 21 cm absorption is filled-in by intervening warm HI emission), along with a high density of foreground stars in 2MASS, Spitzer, or WISE images, and location close to the mid-plane favor the far kinematic distance.

Ellsworth-Bowers *et al.* (2013) have developed an automated statistical distance determination tool that ingests the Galactic latitude, the radial velocity, and Spitzer $8\ \mu\text{m}$ images of the region, and uses an a-priori model of Galactic diffuse $8\ \mu\text{m}$ emission to resolve the KDA using “Distance-Probability Distribution Functions.” This method can be generalized to incorporate star counts and reddening toward dust emission features and the presence or absence of HINSA to provide a product of probabilities for resolving the KDA.

Higher-precision distance assignments will require precision parallax measurements toward associated sources, determination of radial streaming motions, and a full 3D vector model of Galactic rotation. In a few years, visual-wavelength parallax determinations with the GAIA mission will provide distances to sources and so might help with distance determination in relatively nearby regions. “The Bar and Spiral Structure Legacy (BeSSeL) survey” (Brunthaler *et al.*, 2011) will provide direct parallax determinations toward about 400 Galactic sources exhibiting cm-wavelength maser emission, with a precision of $\sim 3\%$ to 10% . BeSSeL will provide direct trigonometric distances throughout the

Galaxy because, unlike the GAIA measurements of stars, radio masers are not subject to extinction.

3. Overview of GMCs on the Large Scale

The mass distribution of GMCs can be described by a power-law $dN/dM \propto M^\alpha$ with a cutoff at about $10^{6.5} M_\odot$ for the Galactic disk (Rosolowsky, 2005). Because $\alpha = -1.5 \pm 0.1$, massive clouds dominate the total mass of H_2 .

GMCs exhibit supersonic internal motions on scales larger than individual star forming cores (~ 0.01 to 0.05 pc). At $R_{gal} > 1$ kpc, tracers such as CO reveal linewidths of order 1 to 10 km s^{-1} in gas of mean density $10^2 - 10^3 \text{ cm}^{-3}$ (Roman-Duval et al., 2010). Dense clumps and cores with $n(H_2) > 10^4 \text{ cm}^{-3}$, traced by high dipole moment dense gas tracers, typically cover only a few percent of the projected surface area of GMCs traced by CO emission. However, in the CMZ such dense gas tracers have line widths of 10 to over 30 km s^{-1} and cover most of the projected surface area traced by CO, indicating that CMZ clouds have one to two orders of magnitude larger mean densities (e.g., Morris and Serabyn, 1996).

Heyer et al. (2009), using FCRAO ^{13}CO data, found a dynamic range of nearly two orders of magnitude in the surface density of the GMCs (a few $10 M_\odot \text{ pc}^{-2}$ to a few $1000 M_\odot \text{ pc}^{-2}$). Their generalization of the classic (Larson, 1981) linewidth-size scaling relation is $\sigma(\ell) \propto \Sigma^{1/2} \ell^{1/2}$. Massive-star forming clumps also appear to follow this relation (Ballesteros-Paredes et al., 2011).

Molecular clouds have internal filamentary structure, first seen in deep photographs of nearby dark clouds (Barnard, 1907) and extensively explored in CO maps, e.g., in Orion and Taurus (Bally et al., 1987a; Narayanan et al., 2008; Kirk et al., 2013b). Widespread filamentary IRDCs, seen in silhouette against the bright mid-IR background of the Galactic Plane (Egan et al., 1998), are of heightened interest because IRDCs are the densest, highest column density parts of GMCs most closely associated with star formation (Carey et al., 2000). Now, thanks to large-scale dust emission surveys with Herschel, it has become apparent that filaments are a ubiquitous feature of the ISM at all size scales. For example, Figures 1 and 2 show Herschel Hi-GAL images of filamentary structure in the W3–5 and $l = 111$ complexes, respectively.

3.1. Formation

Theories of GMC formation have evolved enormously since the discovery of CO. Many of the key considerations are discussed in the review by McKee and Ostriker (2007). The article by Dobbs et al. in this volume also covers the formation of molecular clouds and so here we will simply highlight a few recent developments.

There is growing evidence that GMCs, and the star-forming clumps within them, form in a multi-step process. The first step is the concentration of the diffuse non-molecular ISM, with a mean density of 1 cm^{-3} , into HI superclouds and related Giant Molecular Associations

(GMA) with mean densities of 10 cm^{-3} (Elmegreen and Elmegreen, 1987). GMA are characterized by $10^6 - 4 \times 10^7 M_\odot$ HI halos surrounding GMC complexes at 1 to 2 kpc intervals along the major spiral arms of the Galaxy (Dame et al., 1986). For example, in the Perseus arm of the outer Milky Way, GMA are found at approximately 2 kpc intervals at longitudes $l \sim 110^\circ$ to 112° associated with NGC 7538 (Fallscheer et al., 2013), $l \sim 132^\circ$ to 136° associated with the W3 (Rivera-Ingraham et al., 2013), W4, and W5 giant HII regions, and $l \sim 172^\circ$ to 180° associated with the Sh2-235 HII region. Multi-wavelength Herschel imaging brings out the spectacular structures in such complexes, as illustrated in Figures 1 (W3–W5) and 2 (NGC 7538). The GMA form by the combined effects of self gravity, the gravitational potential of the Galactic plane, and compression by spiral arms (Elmegreen, 1994); they are gravitationally bound with internal motions dominated by turbulence (Dame et al., 1986).

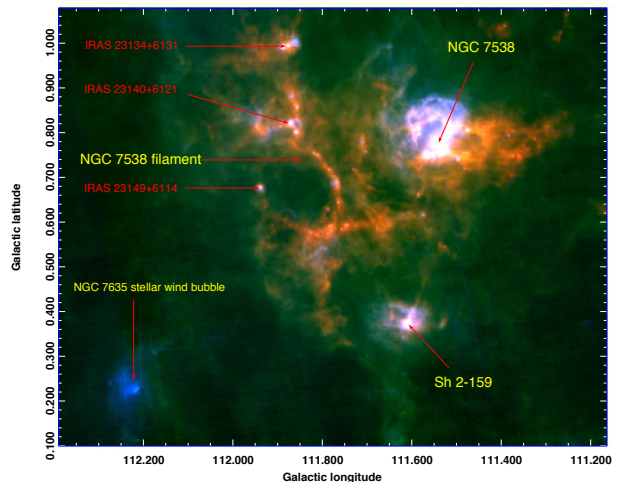


Fig. 2.— Hi-GAL three-color composite of the GMC complex associated with the NGC 7538 HII region at $l = 111$ in the Perseus Arm, from data at $70 \mu\text{m}$ (blue), $160 \mu\text{m}$ (green), and $350 \mu\text{m}$ (red), in Galactic coordinates.

The subsequent steps concern the development of structures of higher density. The second is the formation of dense sheets in post-shock layers where supersonic turbulence, or the shells and bubbles produced by massive-star feedback, produce converging and colliding flows (e.g., Audit and Hennebelle, 2005). The third step is the cooling of the post-shock layers and conversion of predominantly atomic gas into molecular gas. Fourth is the formation of dense filaments from sheets. Fifth is the fragmentation of filaments and sheets into star-forming clumps. Recent theoretical developments and observational evidence concerning filaments and dense clumps formation are discussed in §4.1 and §4.2. At each step, the density is increased by about an order of magnitude, thus reaching $n(H) \sim 10^6 \text{ cm}^{-3}$ in clumps and cores.

It is not yet clear at which step the resulting substructure becomes recognizable as CO-bright molecular clouds. As

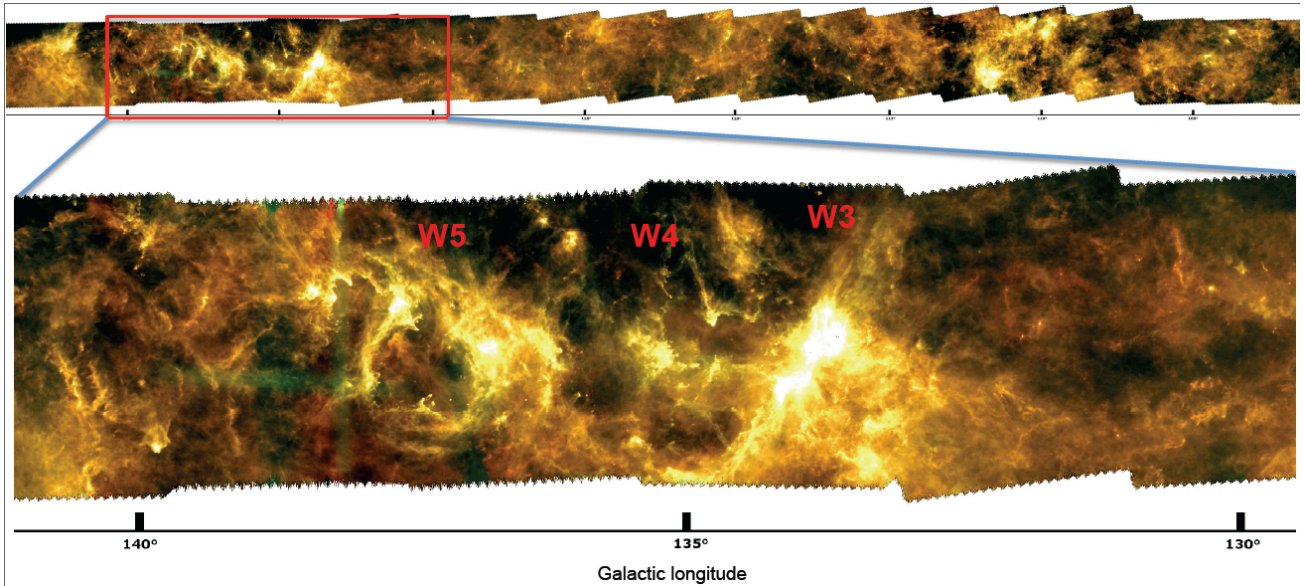


Fig. 1.— Top: Hi-GAL three-color composite of a portion of the Perseus Arm from data at $70\ \mu\text{m}$ (blue), $160\ \mu\text{m}$ (green), and $350\ \mu\text{m}$ (red). Bottom: The W5, W4, and W3 GMA and giant HII region complex near $l = 134^\circ$. The red box outlines this region in the top panel.

discussed below, gravity and supersonic convergence can compress the CO-dark H_2 to sufficient density to produce and excite CO, producing CO-bright structures only shortly before the onset of star formation.

3.1.1. CO-free H_2 ; Dark gas as Fuel for GMC Formation

Aperture synthesis observations of nearby spiral galaxies (Allen *et al.*, 2004; Heiner *et al.*, 2009) comparing their CO and HII region distributions and radial velocities show that most of the gas traced by the 21 cm emission line is located downstream from spiral arms, active sites of star formation, and HII regions. These results provide evidence that this HI might be primarily a photodissociation product. In this picture, GMCs would primarily form from HI clouds *through* CO-dark molecular gas *rather than directly* from HI clouds.

Pringle *et al.* (2001) hypothesized a component of the ISM in which hydrogen is mostly molecular but that is CO-free and not traced by bright CO emission. There is growing observational evidence for such “dark molecular gas” (Wolfire *et al.*, 2010). Comparison of the total hydrogen column density using gamma-ray (Grenier *et al.*, 2005; Abdo *et al.*, 2010) or dust emission (e.g., Planck Collaboration *et al.*, 2011) with maps of 21 cm HI and CO-bright H_2 show that there is significant dark H_2 surrounding most nearby molecular clouds. The mass of such CO-free dark gas might be comparable to the mass of H_2 traced by CO emission. The GOT C^+ survey of the Milky Way disk in the CII $158\ \mu\text{m}$ line also provides evidence for a substantial amount of CO-dark H_2 (Pineda *et al.*, 2013). Additionally, Allen *et al.* (2012) obtained deep 18 cm observations of OH emission in a portion of the Perseus arm, finding abundant OH in regions that do not show detectable CO emission.

H_2 can reach a high equilibrium abundance in the ISM in gas flows that have lower volume and surface densities than those typical of GMCs (e.g., Dobbs *et al.*, 2008). For instance, Clark *et al.* (2012) demonstrate that the formation of CO-bright regions in the gas occurs only around 2 My before the onset of star formation. In contrast, H_2 -dominated but CO-free regions form much earlier. The time scales might be long enough that HI and CO-dark gas can coexist, as evidenced by the massive HI envelopes surrounding the Perseus (Lee *et al.*, 2012) and Taurus molecular clouds (Heiner and Vázquez-Semadeni, 2013). The level of dissociating UV flux is not sufficient to explain all of this HI as a photo-dissociation product, suggesting that these HI envelopes might be converting into CO-dark gas.

3.1.2. Conditioning the ISM Reservoir

Large-scale gravitational instabilities in the Galactic disk can drive GMC formation. Stability of a disk can be quantified in terms of the Toomre parameter (Toomre, 1964) $Q \equiv c_s \kappa / \pi G \Sigma$, where c_s is the sound-speed of the gas, κ is the epicyclic frequency, which is typically of the same order of magnitude as Ω , the rotational frequency of the disk, and Σ is the surface density of the disk. A pure gas disk is gravitationally unstable wherever $Q < 1$. The analysis for a disk that contains both gas and stars is more complex (e.g., Elmegreen, 2011a), but instability still requires a Toomre parameter of order unity.

The question of whether the Milky Way is Toomre stable has been examined recently by Kruijssen *et al.* (2013). They conclude that in the CMZ the gas is marginally unstable, with $Q \sim 1$, only within the central so-called 100-pc ring (see §3.3) revealed by Herschel (Molinari *et al.*, 2011). On

larger scales in the disk, they find stability for $R_{gal} < 4\text{kpc}$. *Kruijssen et al.* (2013) also find that the disk is highly stable at $R_{gal} > 20\text{ kpc}$, due to its low surface density, and although metallicity dependent variations in the CO-to-H₂ conversion factor could lead to this being underestimated (*Glover and Mac Low*, 2011), it is unlikely to make enough of a difference to render the disk unstable.

It is therefore plausible that on the largest scales, gravitational instability helps to gather together the gas required for GMC formation. However, GMCs probably do not form directly from this instability: the growth time scale is long (*Elmegreen*, 2011a), and the applicability of the Toomre analysis, which assumes an infinitely thin disk, to scales smaller than the disk scale height is also questionable. It is far more plausible that gravitational instability promotes GMC formation indirectly, by enhancing non-axisymmetric features such as spiral arms that help to gather the diffuse gas together (e.g., *Dobbs et al.*, 2012), and by directly driving turbulence in this gas (e.g., *Wada et al.*, 2002). Both mechanisms can induce the converging flows that constitute the last stage of compression necessary to form GMCs.

Another form of mass assembly is bubbles created by massive star feedback. Giant HII regions and the collective effects of multiple supernovae in OB associations can sweep up kpc-scale shells which blow out of the disk, and massive, slowly expanding rings of gas in the Galactic plane. The 21 cm surveys of *Hartmann and Burton* (1997) reveal hundreds of HI supershells in the Galaxy surrounding OB associations (*Koo et al.*, 1992; *Ehlerová and Palouš*, 2013). These 0.1 to 1 kpc scale features surround bubbles of hot plasma traced by extremely low density HII regions and X-ray emission. They appear to be powered by the combined impact of photoionization, stellar winds, and supernova explosions. *McCray and Kafatos* (1987) proposed that gravitational instabilities in the supershells swept-up by expanding superbubbles would first occur on the mass-scale of GMCs in the Solar vicinity. As superbubbles sweep-up the surrounding ISM, the resulting shell expansion velocities decrease. Once the local velocity dispersion of a given patch of the shell drops below the gravitational escape velocity, that region becomes subject to gravitational instability. Both small and large length- and mass-scales are stable, giving rise to a critical intermediate scale, which in the Solar vicinity is similar to the observed scales of GMCs.

Regardless of whether it is ultimately gravity or stellar feedback that is more important for assembling diffuse gas into dense clouds, the behavior of the gas on small scales is likely to be rather similar. Because GMC formation requires large amounts of gas to be gathered into one place, GMCs will typically form at the stagnation points of converging flows of gas, and the details of their formation will have little dependence on how these flows are driven.

3.1.3. Large and Small-Scale Converging Flows

The potential importance of converging or “colliding” flows as a GMC formation mechanism was first stressed

by *Ballesteros-Paredes et al.* (1999) and *Hartmann et al.* (2001). The earliest one-dimensional models (e.g., *Hennebelle and Pérault*, 1999; *Koyama and Inutsuka*, 2000) showed that the collision of streams of thermally stable warm gas could increase their density sufficiently to render the gas thermally unstable (*Field*, 1965). The resulting thermal instability leads to a large increase in the gas density from a value $\sim 1\text{ cm}^{-3}$, characteristic of the warm neutral medium (WNM), to $\sim 100\text{ cm}^{-3}$, characteristic of the cold neutral medium (CNM). At the same time, the temperature of the gas falls by two orders of magnitude, from $T \sim 6000\text{ K}$ in the WNM to $T \sim 60\text{ K}$ in the CNM.

Subsequent 2D and 3D modeling demonstrated that the thermal instability occurring in the post-shock gas layer naturally produces turbulence with a velocity dispersion similar to the sound speed in the unshocked gas (e.g., *Koyama and Inutsuka*, 2002; *Heitsch et al.*, 2005; *Vázquez-Semadeni et al.*, 2006; *Banerjee et al.*, 2009). Thermal instability can create dense structures directly via the isobaric form of the instability. However, most of the resulting small clumps are not self-gravitating (*Koyama and Inutsuka*, 2002; *Heitsch et al.*, 2005; *Glover and Mac Low*, 2007), and instead it is the ensemble of clumps produced by a coherent converging flow that might become unstable (*Vázquez-Semadeni et al.*, 2007).

An important feature of the clouds formed in colliding flows is that they typically undergo global gravitational collapse primarily in the directions perpendicular to the flow (see, e.g., *Vázquez-Semadeni et al.*, 2007). Such collapse naturally leads to the formation of filaments. The non-linear development of the thermal instability also proceeds by forming a network of filaments (see §4.1), at whose intersections clumps (see §4.2) are subsequently formed (*Audit and Hennebelle*, 2005; *Vázquez-Semadeni et al.*, 2006; *Heitsch et al.*, 2008).

3.2. Lessons from the Solar Vicinity

Currently, the Sun appears to be located in an inter-arm spur of gas and dust between two major spiral arms of the Galaxy (*Xu et al.*, 2013). The Sun appears to be inside a superbubble. Most of the ISM in the Solar vicinity is expanding with a mean velocity of $2\text{--}5\text{ km s}^{-1}$, discovered in HI and more apparent in molecular gas (e.g., *Lindblad et al.*, 1973; *Dame et al.*, 2001). At the center of “Lindblad’s ring” is the 50 My old Cas–Tau group, a “fossil” OB association (*Blaauw*, 1991), whose most massive members have evolved and become supernovae. The kpc-scale superbubble produced by the Cas–Tau group blew out of the ISM both above and below the Galactic plane. Consistent with ballistic trajectories of dense clouds entrained in or formed from supershells, HI surveys reveal complexes of in-falling gas (*Stark et al.*, 1992; *Kuntz and Danly*, 1996).

The nearest OB associations such as Scorpius–Centaurus, Per OB2, Orion OB1, and Lac OB1b, and the B and A stars that trace the so-called “Gould Belt” of nearby young and intermediate age stars, are all associated with Lind-

blad’s ring (Lesh, 1968; de Zeeuw *et al.*, 1999), evidence for secondary star formation in clouds that condensed from the ancient, expanding, and tidally-sheared supershell (see Figs. 5 and 6 in Perrot and Grenier 2003). These nearby OB associations have spawned their own superbubbles with sizes ranging from 100 to 300 pc. The remaining GMCs in each of these regions are embedded within their respective superbubbles. Thus most of the star-forming molecular clouds in the Solar vicinity have been extensively impacted and processed by massive star feedback from nearby OB associations.

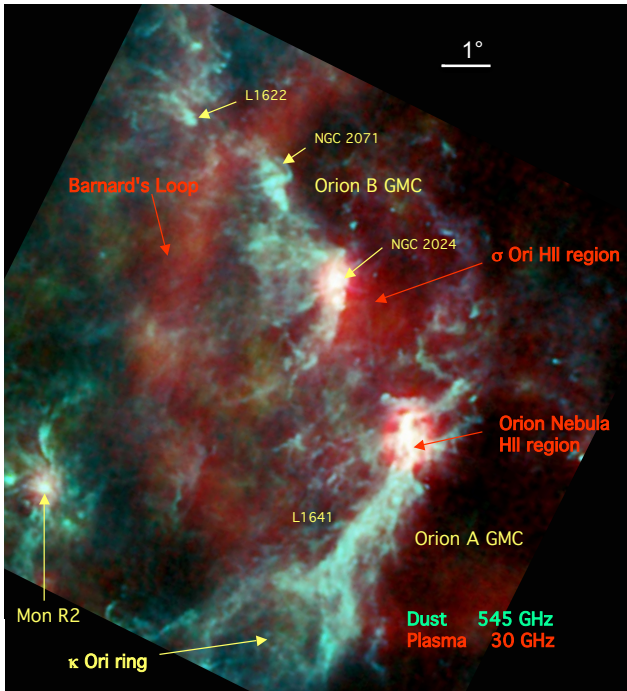


Fig. 3.— Planck view of the $10^5 M_{\odot}$ Orion A and B GMCs, traced by dust continuum emission at 545 GHz (turquoise), and the eastern portion of the Orion-Eridanus superbubble, in free-free emission at 30 GHz (red). The cometary Orion A cloud faces the center of the Orion-Eridanus bubble. The Orion Nebula and the OMC1/2/3 clumps are the most active sites of star formation in the Solar vicinity.

Figure 3, after Bally (2010) and updated using Planck data (Planck Collaboration *et al.*, 2013a), shows the Eastern part of the Orion-Eridanus superbubble in detail. The northern portion of the Orion A cloud hosts the most active site of ongoing star formation within 500 pc of the Sun. The Orion A cloud is cometary with its northern end located toward the projected interior of the superbubble. The Orion Nebula and the OMC1 core, the closest site of active high-mass star formation, is in the center of the degree-long, high-density Integral Shaped Filament (see §4.1.2) (Johnstone and Bally, 1999, 2006).

3.3. Lessons from the Central Molecular Zone

Extending from longitudes $\sim -5^{\circ}$ to $+5^{\circ}$ (Fig. 4), the CMZ provides a unique opportunity to investigate the properties of dense gas in a circumnuclear environment containing a supermassive black hole (SMBH). Approximately 10% of the Milky Way’s ISM lies within 0.5 kpc of the Galactic Center’s SMBH. The CMZ contains the most extreme GMCs and star forming regions in the Galaxy.

The CMZ contains $2 - 6 \times 10^7 M_{\odot}$ of molecular gas with average densities greater than 10^4 cm^{-3} , sufficient to excite most high dipole-moment molecules such as NH_3 , CS, HCN, HCO^+ , and HNC everywhere in the CMZ (Dahmen *et al.*, 1998; Ferrière *et al.*, 2007; Jones *et al.*, 2012). The CMZ GMCs differ from GMCs in the Galactic disk in several ways: 1) They have one to two orders of magnitude higher mean density. 2) High dipole-moment molecules are excited throughout the volume of CMZ GMCs, not just in isolated clumps and cores as in Galactic disk GMCs. 3) CMZ GMCs have larger line-widths (typically 15 to more than 50 km s^{-1}) than disk GMCs (typically 2 to 5 km s^{-1}). Large line-widths are an indication of large-amplitude internal motions. Indeed, Huettemeister *et al.* (1998) found extensive SiO emission from the CMZ clouds, indicating the presence of shocks sufficiently strong to sputter dust grains to produce a significant gas-phase abundance of SiO. Molecular gas in the CMZ is not only dense, but also warm, and able to excite high-J transitions of CO, as well as a variety of high dipole-moment molecules (Martin *et al.*, 2004).

The orbital dynamics of the gas is critical to the evolution. Non-self-intersecting orbits form two families: the x1 orbits whose major axes are aligned with the bar and the x2 orbits which tend to be elongated orthogonal to the bar. The x1 orbits become more “cuspy” as their semi-major axes shrink, eventually becoming self-intersecting. Clouds on such orbits will collide, resulting in loss of orbital angular momentum and settling onto the more compact x2 family of orbits. While the x1 orbits are populated by HI and some molecular clouds, the x2 orbits contain the densest and most turbulent molecular clouds in the Galaxy. Almost all star formation in this gas, heating the warm dust seen as bright blue and green emission in Figure 4, occurs within about 100 pc of the nucleus. The CMZ gas is asymmetrically located with respect to the dynamic center of the Galaxy. Two-thirds of this emission is at positive longitudes and has positive radial velocities; only one-third is at negative longitudes and has negative radial velocities (Bally *et al.*, 1987b, 2010; Jones *et al.*, 2012). Remarkably, the majority of $24 \mu\text{m}$ sources in Figure 4 are located at *negative* Galactic longitudes, not on the side of the nucleus containing the bulk of the dense CMZ gas and associated cold dust (red). Molinari *et al.* (2011) found that the coolest dust and the highest column density gas is located in an *infinity-sign-shaped* ring with a radius of about 100 pc (Fig. 5).

Other notable features are marked in these figures. The Sgr B2 molecular cloud at $l = 0.8^{\circ}$ contains over $10^6 M_{\odot}$ of molecular gas and hosts what might be the most luminous

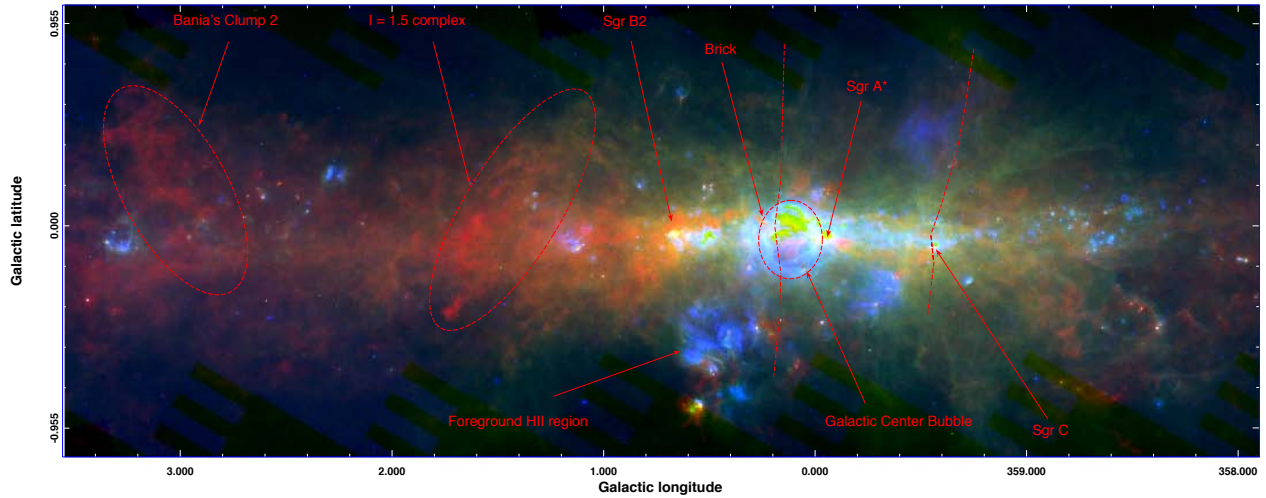


Fig. 4.— The Central Molecular Zone (CMZ) in a composite three-color image combining *Spitzer* 24 μm (blue) with *Herschel* 70 μm (green) and 500 μm (red). Noticeable features are identified in the figure; the Sofue-Handa lobe structure (see text) is delimited by the two nearly vertical red-dashed lines at $l \sim 0.2^\circ$, and $l \sim -0.5^\circ$.

site of massive star formation in the Galaxy. It is located adjacent to the older Sgr B1 region at the high longitude end of the 100 pc ring. Sgr C, located at the negative longitude end of the ring, hosts the second most massive site of star formation in the CMZ.

The prominent oval of warm dust (left of center in the lower panel of Fig. 5) is a very young 30 pc diameter superbubble (the “Galactic Center Bubble” or GCB) whose interior contains the massive, 3 to 5 My old Arches and Quintuplet clusters. The Sgr A region and the SMBH are located outside the GCB; thus the GCB might be powered mostly by massive stars. The GCB is the smallest and brightest member of a set of nested bubbles emerging from the central 100 pc region of our Galaxy. The Sofue-Handa lobe (Sofue and Handa, 1984) is a degree-scale bubble traced by free-free emission blowing out of this region. The relationship between these features and the recently recognized kpc-scale Fermi-LAT-Planck bubble (Su *et al.*, 2010; Planck Collaboration *et al.*, 2013c) remains unclear. Is this bubble powered by the merging of superbubbles fed by dying massive stars in the CMZ, fed by occasional AGN activity of the SMBH, or a combination of these mechanisms?

The compact, high column density clump of cold dust located to the left of the GCB (“Brick” in Figs. 4 and 5) is the most extreme IRDC in the Galaxy (Longmore *et al.*, this volume). This clump is located in the 100 pc ring, has a mass greater than $10^5 M_\odot$ within a radius of 3 pc, yet shows no evidence of any star formation (Longmore *et al.*, 2012). It is part of a string of massive clouds stretching from a location near Sgr A* to Sgr B2, including several with various degrees of on-going star formation, possibly triggered by a close passage near the SMBH (Longmore *et al.*, 2013a).

Wide-field mapping of the CMZ in the dust continuum, high-J CO lines, the CI line, and a variety of dense gas tracers will shed light on a number of critical questions

about star formation, the ISM, and its interactions with the SMBH. Does nuclear star formation shield the central black hole from growth? Or does occasional flaring of the SMBH regulate the state of the ISM and star formation in the CMZ? What is the star formation rate in the CMZ? Does it follow the Schmidt-Kennicutt relation, or is the star formation rate per unit mass of dense gas lower in the CMZ than in galactic disks (Longmore *et al.*, 2013b; Kruijssen *et al.*, 2013)?

4. Converting GMCs to Dense Structures

It is well established that only a small fraction of the gas in GMCs is dense enough to be involved in star formation. This is apparent from CS surveys in high-mass star forming regions (e.g., Plume *et al.*, 1992, 1997), as well as from large-scale gas and dust mapping of nearby low-mass star forming regions (e.g., Goldsmith *et al.* 2008).

Herschel surveys allow investigation of the properties of IRDCs because the cold and dense dust shines brightly in the submm continuum. Visual inspection by Wilcock *et al.* (2012) of the Hi-GAL survey in the $300^\circ \leq l \leq 330^\circ$ region of the Galactic Plane suggests that only 50% of the Peretto and Fuller (2009) IRDCs are *bona fide* cold and dense structures while the rest are regions devoid of background mid-IR emission. Nevertheless, the Peretto & Fuller column densities derived from the mid-IR opacity provide independent measurements that can be compared with estimates obtained from Herschel’s complete far-IR photometric coverage (Elia *et al.*, 2013, 2014; Schisano *et al.*, 2014).

Unbiased surveys allow statistically significant estimates of the lifetimes and relative durations of the various stages of evolution of clouds, clumps, and cores. For example, Tackenberg *et al.* (2012) use a portion of the ATLASGAL survey to estimate the time scale for massive starless clumps using association to GLIMPSE sources, obtaining quite short ($6\text{--}8 \times 10^4$ y) time scales. Wilcock *et al.* (2012) anal-

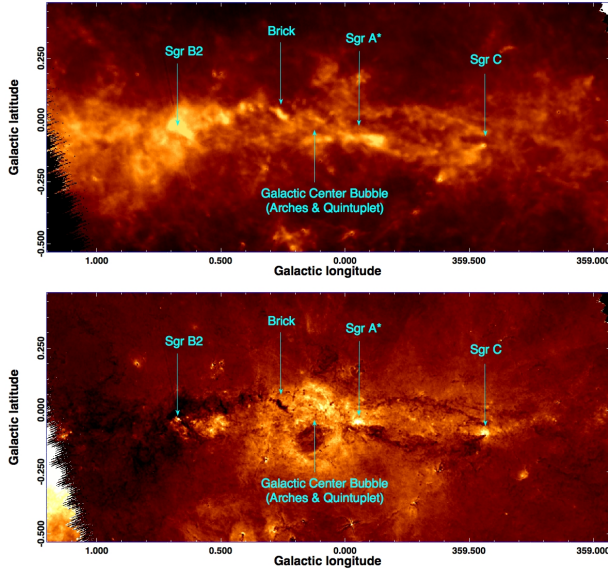


Fig. 5.— Maps of background-subtracted dust column density (upper) and dust temperature (lower) from Hi-GAL images (Molinari *et al.*, 2011) of the inner $2^{\circ}2$ of the CMZ. Large regions of cold dust are associated with Sgr B2 (left), Sgr C (right), and the 20 km s^{-1} cloud (right of center). The warm Galactic Center Bubble is to the left of Sgr A.

use a portion of the Hi-GAL survey and find that only 18% of the Peretto & Fuller *bona fide* IRDCs in the $300^{\circ} \leq l \leq 330^{\circ}$ range appear not to be associated with either 8 or $24 \mu\text{m}$ counterparts.

An interesting approach has been adopted by Battersby *et al.* (2011), in which Hi-GAL column density and temperature maps in the $l=30^{\circ}$ and $l=59^{\circ}$ fields were compared to companion maps in which each pixel is populated with a variety of star formation indicators, including 8 and $24 \mu\text{m}$ emission, association with methanol masers and Extended Green Objects suggestive of the presence of outflows. A pixel-to-pixel comparison showed that pixels with more star formation indicators have higher column densities and higher temperatures with $T_{\text{dust}} > 20 \text{ K}$.

4.1. Filaments

Surveys with Herschel reveal that the densest regions in molecular clouds are organized in complex filamentary structures (Molinari *et al.*, 2010a). As discussed above and by André *et al.* (this volume), nearby clouds such as Taurus and Ophiuchus are filamentary and Hi-GAL reveals similar structures on much larger scales (several to tens of parsecs) along the Galactic Plane. The ISM is permeated by a web of filamentary structures from very low column density “cirrus” emission to gravitationally “supercritical” clouds, and from the small scales of star-forming cores to scales of tens to hundreds of parsecs in the Galactic Plane.

PACS and SPIRE maps at $70 - 500 \mu\text{m}$ showed that the Aquila Rift and the Polaris Flare contain an extensive network of filaments, many of which are several pc in

length (André *et al.*, 2010). In IC 5146 Arzoumanian *et al.* (2011) show that the filaments have radial density profiles that fall off as $r^{-1.5}$ to $r^{-2.5}$ and mean FWHM widths of $0.10 \pm 0.03 \text{ pc}$. This is much narrower than the distribution of Jeans lengths which range from $\sim 0.02\text{--}0.3 \text{ pc}$. Because the filament widths are within a factor of two of the sonic scale at which the turbulent velocity dispersion equals the sound speed, they suggest that large scale turbulence could be responsible for forming the filaments whereas gravity then drives their evolution by accreting material from the surroundings. This idea seems to be at least circumstantially supported by Chapman *et al.* (2011) whose polarization map of the L1495/B213 filament shows a number of sub-filaments oriented perpendicular to the main filament, but aligned with the magnetic field direction as measured in the surrounding material. These sub-filaments might be related to mass accretion onto the main filament (Palmeirim *et al.*, 2013) which, in turn, might help to form the dense cores within (Hacar and Tafalla, 2011).

Fischera and Martin (2012b,a) discuss equilibrium models of filaments as isothermal self-gravitating infinite cylinders in pressure equilibrium with the ambient medium. These offer an analytical and quantitative explanation of the radial profiles and the width–column-density relation. However, there is a maximum mass line density $M_{\text{lin,max}}$ beyond which there is no equilibrium solution (often referred to as “critical”). If the filaments have only thermal support, then at 10 K $M_{\text{lin,max}} \sim 16 M_{\odot} \text{ pc}^{-1}$, corresponding to a maximum column density of $N_{\text{H}_2,\text{max}} \sim 10^{22} \text{ cm}^{-2}$ or $A_{\text{V,max}} \sim 10$. Note that if there were in addition *turbulent* support, as seems relevant to accreting filaments, then a quasi-static state might exist with higher M_{lin} . Filaments close to, or exceeding, $M_{\text{lin,max}}$ are subject to fragmentation into self-gravitating prestellar cores (Fischera and Martin, 2012b). Given the derived *dust* temperature in these filaments, and assuming that the gas temperature is similar, André *et al.* (2010) find that 60% of the bound (self-gravitating) prestellar cores in these regions are located in filaments with $M_{\text{lin}} > M_{\text{lin,max}}$, indicating a strong association of supercritical filaments and star formation. On the other hand, while filaments with $M_{\text{lin}} < M_{\text{lin,max}}$ interestingly contain cores, few of these cores have strong self-gravity.

Herschel has shown that filamentary structures are organized into complex interconnected branches and also loops. Examples include the Vela region (Hill *et al.*, 2011) and DR21 (Schneider *et al.*, 2010a). The first results from the Hi-GAL survey showed widespread filamentary structures on larger scales in a $2^{\circ} \times 2^{\circ}$ region toward $l = 59^{\circ}$ (Molinari *et al.*, 2010a). Like André *et al.* (2010), they find that dense cores/clumps tend to be associated with the filaments. They find that the column densities of the filaments lie in the range $10^{21} \text{ cm}^{-2} \leq N(\text{H}_2) \leq 10^{22} \text{ cm}^{-2}$, corresponding to $1 \leq A_{\text{V}} \leq 10$. This range is lower than found for local clouds like the Aquila Rift (distance 260 pc) and the Polaris Flare (150 pc) and could be due in part to the greater distances of the filaments in the $l = 59^{\circ}$ region ($\sim 2\text{--}8 \text{ kpc}$)

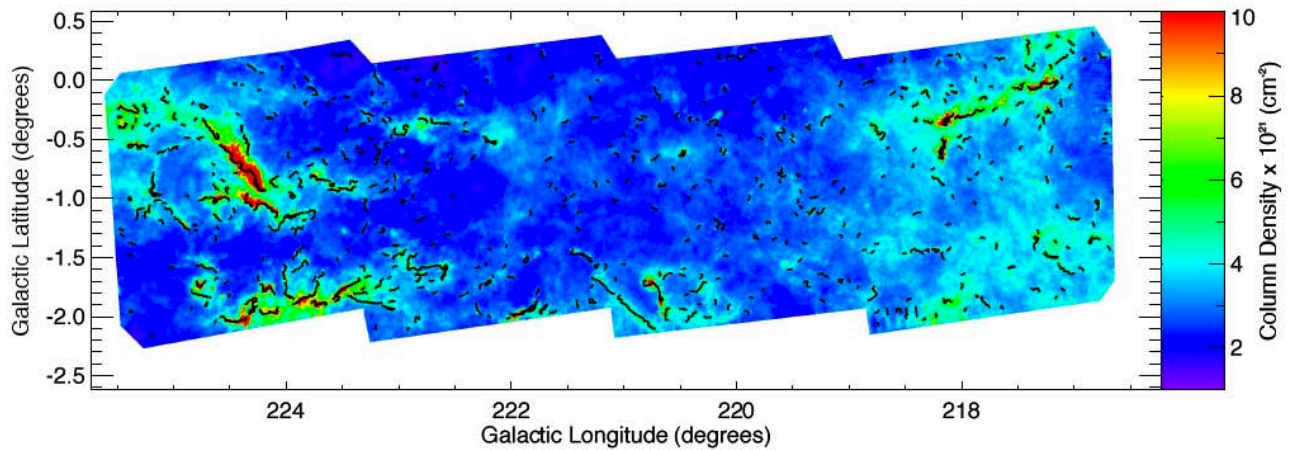


Fig. 6.— Column density map from Hi-GAL images in the Galactic longitude range $217^\circ \leq l \leq 224^\circ$ (Elia *et al.*, 2013). The thick black lines delineate the main spine of each detected filament (branches are neglected for clarity). Detected filaments are those that show a contrast greater than three times the standard deviation of the column density computed locally.

and the resulting beam dilution (at these distances, Hi-GAL also detects clumps instead of cores).

More rigorous detection and quantitative assessment of filaments is now underway using a variety of tools based on a variety of morphological analyses of multi-scale diffuse emission. One of these approaches is based on the analysis of the Hessian matrix computed over large-scale column density maps (but see also Arzoumanian *et al.* 2011), and it has been applied by Schisano *et al.* (2014) over an $8^\circ \times 2^\circ$ Hi-GAL column density map of the Galactic Plane over the longitude range $l = 217^\circ - 224^\circ$. They identified over 500 filaments (with ~ 2000 branches) with lengths from 1.5–9 pc and column densities from 10^{19} to 10^{22} cm^{-2} (see Fig. 6). Again, these column densities are lower than those cited by André *et al.* (2010) for two possible reasons: beam dilution caused by the greater distances to these filaments (500 pc – 3.5 kpc) and the fact that Schisano *et al.* (2014) use the average column density rather than the column density at the spine of the filaments. This latter effect tends to decrease the quoted column density by a factor of four. Focusing on only the nearest filaments, they find average lengths, widths, and column densities to be 2.6 pc, 0.26 pc, and 9.5×10^{20} cm^{-2} , respectively. Nevertheless, these filaments are still wider and less dense than those in Arzoumanian *et al.* (2011) by a factor of 2–3, and so not all demonstrably supercritical.

The analysis of Schisano *et al.* (2014) also deals with the physical properties of what they call the individual “branches” of the filamentary networks, i.e., the subportions of filamentary structures limited by the nodal points created by the intersections. They found that the branches containing protostellar clumps have $M_{\text{lin}} \sim 20 - 30 M_\odot \text{ pc}^{-1}$ (arguably supercritical), whereas branches with only prestellar clumps have $M_{\text{lin}} \sim 4 M_\odot \text{ pc}^{-1}$. Although “prestellar” clumps are simply those with no coun-

terpart in the Hi-GAL $70 \mu\text{m}$ band, the absence of associated $70 \mu\text{m}$ emission is an indication of considerably lower rates of star formation than found in protostellar clumps containing detectable $70 \mu\text{m}$ sources.

4.1.1. Filament Formation Mechanisms

There are a number of physical mechanisms that can form filamentary structure. These include gravity, compressive flows in supersonic turbulence and colliding sheets, production of tails by shadowing by dense clumps (the pillars of M16 are a well-known example), fragmentation of expanding shells and supershells, generation of fingers through Rayleigh-Taylor instability, and magnetic fields.

Gravity: Lin *et al.* (1965) demonstrated that spheroidal gas clouds tend to flatten as they collapse, yielding sheet-like structures, and sheets collapse into filaments (see also Larson, 1985). To produce sheets and filaments, the mass of the collapsing cloud must be much larger than the Jeans mass, because in clouds with masses close to M_J , isotropic pressure forces tend to keep the clouds quasi-spherical.

Supersonic turbulence: Both purely hydrodynamic (HD) and magnetohydrodynamic (MHD) supersonic turbulence can lead to filament formation (e.g., Padoan *et al.*, 2001). Supersonic turbulence creates a complex network of shocked-layers confined by the ram pressure of the convergent parts of the flow. The supersonic collision between shock-formed sheets produces denser filaments. If these shock-compressed layers become sufficiently massive, their self-gravity can lead them to collapse. Otherwise, they will tend to dissolve on a turbulent crossing time. The Mach number of the turbulence determines the density contrast ρ_2/ρ_1 between pre- and post-shocked gas: for HD shocks, this scales as \mathcal{M}^2 , where the Mach number $\mathcal{M} = V/c_s$. For MHD shocks, $\rho_2/\rho_1 \approx \mathcal{M}$ (Padoan and Nordlund, 2002), with \mathcal{M} being given by V/c_A in this case. Here,

c_s is the sound speed and $c_A = B/(4\pi\rho)^{1/2}$ is the Alfvén speed. Highly supersonic turbulence therefore yields high density contrasts, while transonic or subsonic turbulence creates only small perturbations that then must be amplified by some other mechanism, such as gravity. The mass accumulated in post-shock layers depends on the correlation length of the turbulent velocity field; larger correlation lengths imply higher mass accumulation layers.

Both gravity and supersonic turbulence formation mechanisms work more readily in cold and dense gas with a low sound (or Alfvén) speed and small Jeans mass. Therefore the thermal evolution of the gas plays an important role. Rapid and efficient cooling can lead to non-linear development of thermal instability that can enhance filament formation (e.g., *Vázquez-Semadeni et al.*, 2000, 2006; *Heitsch et al.*, 2005). Which of these processes (gravity, turbulence or thermal instability) is primarily responsible for the formation of the filaments observed in the ISM remains undetermined; plausibly, all three processes could play important roles. Nevertheless, recent simulations (e.g., *Gómez and Vázquez-Semadeni*, 2013) suggest that large-scale gravitational collapse plays the dominant role here.

Shadowing and cometary clouds: Many HII regions exhibit cometary clouds with long filamentary tails pointing away from the direction of ionization. For example, Figure 1 shows several cometary clouds and filamentary tails in the W4 and W5 giant HII regions. Figure 3 shows that the entire Orion A cloud is cometary with streamers trailing away from the dense Integral Shaped Filament containing the Orion Nebula Cluster and the OMC1, 2, and 3 cloud cores which together have spawned over 2,000 YSOs in the last few My.

Fragmentation of expanding shells and supershells: Bubbles created by the non-ionizing radiation field of late B and A stars and HII regions as well as superbubbles and supernova remnants can sweep-up ambient gas into expanding shells (see §3.1.2). Limb brightening of the shells at the edges can make them look filamentary. Hi-GAL data reveals many approximately circular or semi-circular filaments such as shown in Figure 2. Additionally, various hydrodynamic instabilities such as the Vishniac or Rayleigh-Taylor instability, or the over-running of dense clumps can lead to filamentary structure. The presence of a regular entrained magnetic field can also confine the motion of the charged component, thereby breaking the symmetry to produce filamentary structure.

Rayleigh-Taylor instability: Rayleigh-Taylor (RT) instabilities occur when a dense fluid overlies a light fluid, or when there is an acceleration of a light fluid through a dense layer. When the shock fronts associated with expanding giant HII regions or superbubbles reach radii comparable to or larger than the scale-height of the Galactic gas layer, they can accelerate as they encounter an exponentially decreasing density profile. Additionally, ionization fronts propagating in a density profile that decreases faster than r^{-2} tend to become RT unstable. The RT instability creates long fingers of dense material oriented parallel to the pressure or

density gradient, with the appearance of elongated, filamentary, cometary clouds. Dense clouds located more than a few scale heights above the Galactic mid-plane tend to become elongated orthogonal to the plane due to the effect of superbubbles breaking out of the Galactic gas layer.

Magnetic fields: In the Taurus clouds, interstellar polarization of background stars reveals that the minor filaments that run orthogonal to the dense Taurus filaments (*Goldsmith et al.*, 2008) are parallel to the direction of the field over most of the Taurus constellation. This morphology suggests that the charged component of the gas associated with the minor filaments is magnetically confined. The charged component is free to stream along the magnetic field lines and prevented from crossing field lines, instead gyrating about the field. Ion-neutral collisions effectively couple the neutral atoms and molecules to the field.

4.1.2. Filament Substructure

Filaments are observed to have compact substructures consisting of clumps and cores (*Schneider and Elmegreen*, 1979; *Myers*, 2009; *André et al.*, 2010; *Molinari et al.*, 2010b), as expected at least for those that are strongly self-gravitating (with M_{line} near or exceeding $M_{line,max}$), but actually present in most.

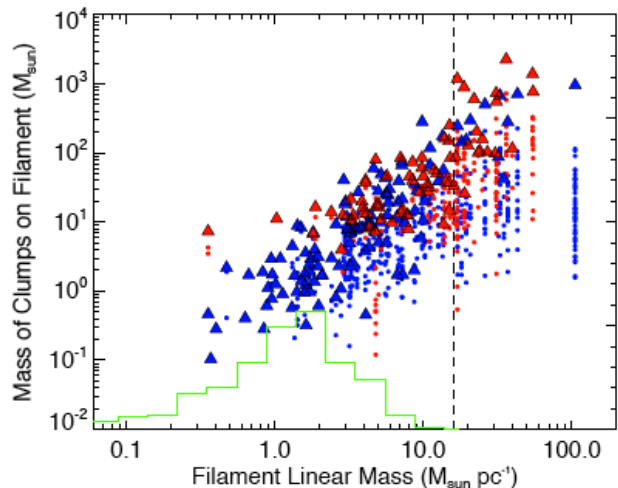


Fig. 7.— Mass of the clumps located in detected filaments in the $l = 217^\circ - 224^\circ$ Galactic plane region (*Schisano et al.* 2014, Fig. 6) vs. M_{line} of the hosting filament. Small dots are individual clump masses, in red for distance $d > 1.5$ kpc and blue for $d \leq 1.5$ kpc. Triangles depict the total mass in clumps on that filament. The distribution of M_{line} for filaments without clumps is also reported in green. The vertical dashed line marks $M_{line,max} \sim 16 M_\odot \text{ pc}^{-1}$ for $T \sim 10$ K.

Figure 7 shows a clear relationship between the masses of the clumps and M_{line} of the filaments hosting them. M_{line} ranges over more than two orders of magnitude and the relationship extends well above $M_{line,max}$ (*Schisano et al.*, 2014). This correlation might indicate that a spectrum of filament mass line densities is produced by large-

scale turbulence or gravitational collapse, with clumps almost immediately fragmenting so that their mass distribution would tend to carry memory of the gravitational state of the parent filament.

Alternatively, the correlation might result from evolution of filaments and clumps toward larger masses as accretion continues from the surrounding environment. Observations suggest continuous flow *onto* filaments as well as from filaments onto cores (Schneider *et al.*, 2010a; Kirk *et al.*, 2013a). Numerical simulations of non-equilibrium collapsing clouds show similar behavior (Gómez and Vázquez-Semadeni, 2013). In such dynamical evolution, filaments fragment into denser clumps that collapse on shorter time scales than the filaments because of different dimensionality: collapse time scales for finite filaments are longer than the clump free-fall time by a factor depending on their aspect ratio (Toalá *et al.*, 2012; Pon *et al.*, 2012). This implies that the clumps begin forming stars before the filaments have finished funneling the entire reservoir of gas onto the cores.

The kinematics of the Integral Shaped Filament (ISF) in the Orion A molecular cloud that contains the Orion Nebula Cluster (ONC; Fig. 3) exhibits this behavior. The ~ 7 pc ($60'$) long and 0.2 pc wide ISF exhibits a velocity jump of 2 to 3 km s^{-1} at the position of the OMC1 cloud core located immediately behind the Orion Nebula. The southern half of the ISF has a radial velocity of $V_{LSR} \approx 8 \text{ km s}^{-1}$ while just north of OMC1 V_{LSR} jumps to about 10 km s^{-1} ; V_{LSR} increases to over 12 km s^{-1} near the northern end of the filament adjacent to the NGC1977 HII region (Ikeda *et al.*, 2007). Despite the unknown projection effects, this velocity jump near the location of the Orion Nebula appears to be similar to the escape velocity with respect to the mass of the OMC1 cloud core and the ONC at a radius of 1 pc from the cluster core, about 3 km s^{-1} . Thus, it seems likely that material in the ISF is being drawn along its length by the gravity of the ONC and the adjacent OMC1 core. If this picture is correct, then the smaller OMC2 and OMC3 clusters might be dragged into the ONC, helping to fuel continued growth of the stellar population there. The time scale for such a merger is roughly 1 My, longer than the crossing time of the ONC (< 0.3 My) or the OMC1 core (< 0.05 My).

The histograms of M_{line} in Figure 8 show systematic differences depending on the presence of prestellar to protostellar clumps. If the filament branches with prestellar clumps are to evolve into the branches with protostellar clumps, then they would have to accumulate enough mass for an order of magnitude increase in M_{line} within only the prestellar core lifetime of a few times 10^5 years, channeling a fraction of this material onto the clumps, thus increasing their mass too. This would imply extremely high accretion rates of the order of $\sim 10^{-3}/10^{-4} M_{\odot} \text{ pc}^{-1} \text{ y}^{-1}$ from the surrounding environment and along the filament branches. Orion’s ISF has a mass of order $3 - 5 \times 10^3 M_{\odot}$. An accretion time scale of 1 My implies an accretion rate into the ONC of about $3-5 \times 10^{-3} M_{\odot} \text{ y}^{-1}$. Such rates, al-

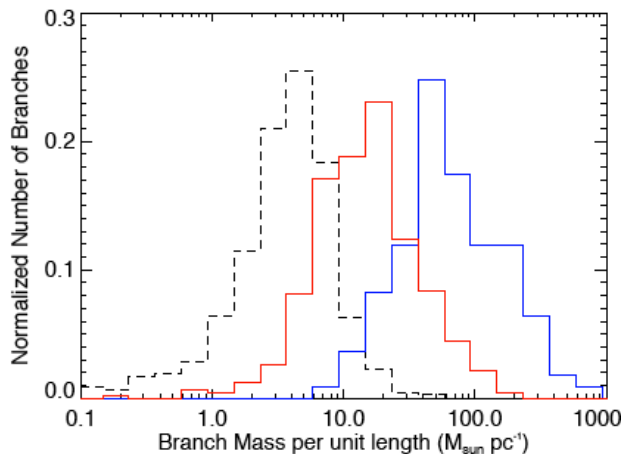


Fig. 8.— Histograms of M_{line} of filament branches detected by Schisano *et al.* (2014): with protostellar clumps (blue solid line), with prestellar clumps (red line), and without clumps (black dashed line). Among the latter, those with higher M_{line} are part of more complex filaments that host both prestellar and protostellar clumps. The histograms have been normalized to the respective total number of filaments to emphasize intrinsic differences between the distributions.

though high, seem consistent with recent observations of the SDC335.579-0.272 cloud by Peretto *et al.* (2013). In this scenario, filaments such as the ISF are long-lived entities that become denser and more massive over time.

Schisano *et al.* (2014) find no correlation between M_{line} of a branch and the clump formation efficiency within that branch. However, the L/M ratio of protostellar clumps increases with M_{line} , suggesting that the increased M_{line} in branches containing protostellar clumps results in an increased star formation rate. Contrary to previous proposals, M_{line} might not always trace the evolution of a filament. When filaments form from large-scale turbulence, many might be transient objects, with only those that are strongly self-gravitating forming stars.

4.2. Clumps

4.2.1. Observed properties

Clumps and cores have been the subject of star formation studies for decades (see, e.g., Lada *et al.* 2007 or the reviews by Andre *et al.* and Offner *et al.* in this volume). In nearby clouds, the core mass spectrum closely resembles the stellar IMF (Motte *et al.*, 1998; Alves *et al.*, 2007), leading to arguments that it determines the IMF. Such detailed studies are limited to low-mass objects, less than about $10 M_{\odot}$. Estimates toward more distant massive clumps are less definitive due to the relatively limited spatial resolution available until now for large samples (Shirley *et al.* 2003; Reid and Wilson 2005; Beltrán *et al.* 2006).

Herschel-based studies by Schisano *et al.* (2014) show that denser clumps are preferentially found on filamentary

structures along the Galactic Plane (see Fig. 9), similarly to what is found at smaller scales in Aquila (*André et al.*, 2010) or toward Orion A (*Polychroni et al.*, 2013). Furthermore, the denser and more massive clumps are preferentially located at the intersection of filaments (*Myers*, 2009; *Schneider et al.*, 2012), indicating that such extreme clumps form from the funneling of gas along filaments.

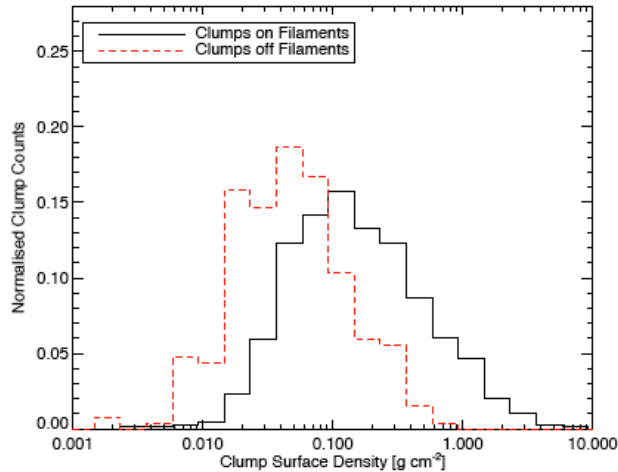


Fig. 9.— Clump surface density distribution for clumps located within filaments (black solid line) or outside of filaments (red dashed line) (from *Schisano et al.* 2014).

Unbiased surveys of the Galactic Plane such as ATLASGAL, BGPS, and Hi-GAL are revolutionizing our understanding of the formation and star-forming evolution of dense protocluster-forming clumps. The ATLASGAL survey (*Schuller et al.*, 2009; *Contreras et al.*, 2013) has been matched to the methanol multibeam (MMB) survey (*Urquhart et al.*, 2013a), identifying 577 submm continuum clumps with maser emission in the longitude range $280^\circ \leq l \leq 20^\circ$ (within 1.5° of the Galactic mid-plane). 94% of methanol masers are associated with submm dust emission and are preferentially associated with the most massive clumps. These clumps are centrally condensed, with envelope structures that appear to be scale-free, and the mean offset of the maser from the peak submm column density is $0'' \pm 4''$. Assuming a Kroupa IMF and a star-formation efficiency of $\sim 30\%$, they found that over two-thirds of the maser-associated clumps are likely to form stellar clusters with masses $\geq 20 M_\odot$ and that almost all clumps satisfy the empirical mass-size criterion for massive star formation (*Kauffmann and Pillai*, 2010). *Urquhart et al.* (2013a) find that the star formation efficiency is significantly reduced in the Galactic Center region compared to the rest of the survey area where it is broadly constant, and that there is a significant drop in the massive star formation rate density in the outer Galaxy. *Longmore et al.* (2013b) compared the absolute star formation rate derived from WMAP free-free emission with the surface density of dense gas and dust from HOPS and Hi-GAL, also deducing a much lower star formation efficiency toward the CMZ.

A further association of ATLASGAL and UCHII regions detected by the CORNISH survey of the inner Galactic Plane (*Purcell et al.*, 2012; *Hoare et al.*, 2012; *Urquhart et al.*, 2013b) identified a lower envelope of 0.05 g cm^{-2} for the surface density of molecular clumps hosting massive star formation and found that the mass of the most massive embedded star is closely correlated with the mass of the associated clump. They find little evolution in the structure of the molecular clumps between the methanol-maser and UCHII-region phases. The value above is significantly lower than the theoretical prediction of 1 g cm^{-2} as a surface density threshold for massive star formation originally proposed by *Krumholz and McKee* (2008), and below the value of 0.2 g cm^{-2} recently proposed by *Butler and Tan* (2012) analysing GLIMPSE counterparts toward a sample of IRDCs.

The 1.1 mm Bolocam Galactic Plane Survey (BGPS) (*Aguirre et al.*, 2011; *Ginsburg et al.*, 2013) identified over 8,500 clumps in the northern Galactic plane (*Rosolowsky et al.*, 2010). BGPS observations of the CMZ can be used to derive a clump mass spectrum for the central 500 pc region (*Bally et al.*, 2010). Using various assumptions about the dust temperature to derive masses, *Bally et al.* (2010) deduce clump mass spectra with a slope $\alpha = 2.4$ to 2.7 ($dN/dM \propto M^{-\alpha}$) in the mass range 10^2 to $10^4 M_\odot$, somewhat steeper than found for nearby low-mass cores or the stellar IMF.

Motivated by the detection of the $10^5 M_\odot$ CMZ cloud dubbed the ‘Brick’, which appears to be nearly devoid of star formation despite its high mass and density, *Ginsburg et al.* (2012) searched in a region excluding the CMZ for massive clumps with sufficient mass to form a young massive cluster (YMCs) with stellar mass of about $10^4 M_\odot$, similar to the masses of the most massive Galactic clusters such as NGC 3603 or Westerlund 1. Under the assumption that the SFE is about 30%, *Ginsburg et al.* (2012) mined the BGPS clump catalog for clumps with masses larger than $5,000 M_\odot$, also requiring the radius to be smaller than 2.5 pc. The latter criterion was based on the arguments presented by *Bressert et al.* (2012) that to form a massive, gravitationally bound cluster, the gravitational escape speed from the cloud had to exceed the sound-speed in photoionized plasma, about 10 km s^{-1} . All of the 18 massive candidate protocluster clumps were found to be actively forming massive stars or clusters based on their IR properties. Most of these massive clumps are associated with well-known giant HII region/star-forming complexes such as W43, W49 and W51. *Ginsburg et al.* (2012) concluded that the duration of any quiescent ‘prestellar’ or ‘precluster’ phase of massive protocluster clumps (MPCCs) must have a duration less than about 0.5 My. Thus, massive clusters in the Galactic disk might be assembled from smaller already actively star-forming units, rather than arising from an isolated massive MPCC (*Longmore et al.*, this volume).

Hi-GAL will greatly increase the number of dense clumps detected. From the first release of Hi-GAL photometric compact sources catalogues *Molinari et al.* (2014a),

more than 5×10^5 individual band-merged entries can be combined for the inner Galaxy only. Downselection to sources with at least 3 detection in adjacent bands delivers an initial catalogue of nearly 100 000 compact sources in the range $+67^\circ \geq l \geq -70^\circ$; for nearly 60 000 of them a distance could be tentatively assigned, allowing to estimates sizes ranging from 0.1 to above 1 pc and masses up to and in excess of $10^5 M_\odot$ (Elia *et al.*, 2014). Dust temperatures range from 7 to 40 K with a median ~ 12 K, below the value of 20 K that is often adopted to derive masses from submm data (Urquhart *et al.*, 2013a) and in better agreement with the ammonia temperature (Wienen *et al.*, 2012) measured toward 862 dense ATLASGAL $870 \mu\text{m}$ clumps. Preliminary studies of the clump mass functions in two very different Hi-GAL fields, toward the near tip of the Galactic Bar and toward the Vul OB1 region ($l = 59^\circ$), show very similar slopes (above the completeness limits) between 1.8 and 1.9 but very different mass scales (Olmi *et al.*, 2013). The much higher sensitivity of Hi-GAL with respect to BGPS or ATLASGAL, and its higher spatial resolution for $\lambda \leq 250 \mu\text{m}$, enable larger statistical samples for clumps that may be hosting massive star formation. Fig. 10 reports the mass-radius relationship for Hi-GAL clumps limited to the lines of sight towards the tips of the Galactic Bar (Veneziani *et al.*, 2014). Clumps extend over areas of the plot where conditions are suited for massive star formation according to a variety of prescriptions. The green solid and the purple dashed areas are the loci with surface densities higher than 1 g cm^{-2} (Krumholz and McKee, 2008) and 0.2 g cm^{-2} (Butler and Tan, 2012), respectively.

Larger statistical samples also allow to improve searches for potential precursors of young massive clusters, that according to Bressert *et al.* (2012) should populate the yellow area in fig. 10. While none of the clumps revealed at the location of the tips of the Bar seem to fulfill this criterium, other regions of the Plane seem to contain such candidates. Figure 11 shows surface density vs. mass for the nearly 60,000 Hi-GAL clumps in the inner Galaxy for which distance estimates exist (Elia *et al.*, 2014), in the context of other structures as reported by Tan (2005). The clumps lie in the area familiar for “Galactic clumps,” and extend beyond it toward surface density above 5 g cm^{-2} and mass well above the $\text{few-}10^4 M_\odot$, to the right of the dashed line marking bounded ionised gas (Bressert *et al.*, 2012), typical of progenitors of the most massive Galactic clusters. For example using the same mass criteria as Ginsburg *et al.* (2012) but with a more stringent threshold of 5 g cm^{-2} in mean clump surface density, more than 100 objects are selected in Hi-GAL (Pezzuto *et al.*, 2014).

4.2.2. Theory

Until recently, most workers considered roundish clumps and cores in isolation as the typical sites of star formation (see, e.g., the reviews by Beuther *et al.*, 2007; di Francesco *et al.*, 2007; Lada *et al.*, 2007; Ward-Thompson *et al.*, 2007), and modeled them as thermally-supported,

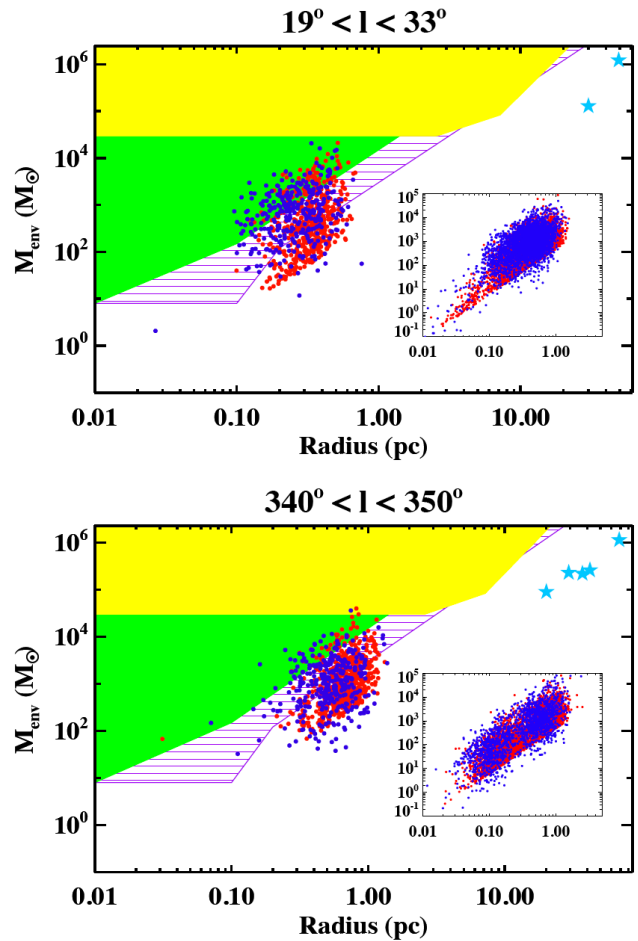


Fig. 10.— Mass vs. radius for the Hi-GAL dense clumps in two ranges of Galactic longitude containing the tips of the Galactic Bar from Veneziani *et al.* (2014). Protostellar (i.e. with $70 \mu\text{m}$ counterpart, blue dots) and prestellar (i.e. without $70 \mu\text{m}$ counterpart, red dots) clumps at the location of the tips of the Bar are reported in the main plots of the two panels. Embedded boxes show the same trend for the rest of the sample in the reported lines of sight. Light blue stars on the top right corner show where GMC present in this area are found (see Veneziani *et al.* 2014). See text for a description of the coloured and shaded areas.

equilibrium Bonnor-Ebert spheres, perhaps undergoing oscillations. However, since the last *Protostars and Planets* volume, it has been realized that cores are highly clustered, and most of them are embedded in filaments from which they accrete (Myers, 2009; André *et al.*, 2010; Molinari *et al.*, 2010b; Arzoumanian *et al.*, 2011; Kirk *et al.*, 2013a).

In turbulent models of GMCs, transient density fluctuations produced by shocks with sufficient compression and mass to exceed the Jeans mass result in gravitationally-bound clumps and cores, while simultaneously providing support for the clouds as a whole (see, e.g., the review by Ballesteros-Paredes *et al.*, 2007, and references therein). However, recent simulations of molecular cloud formation

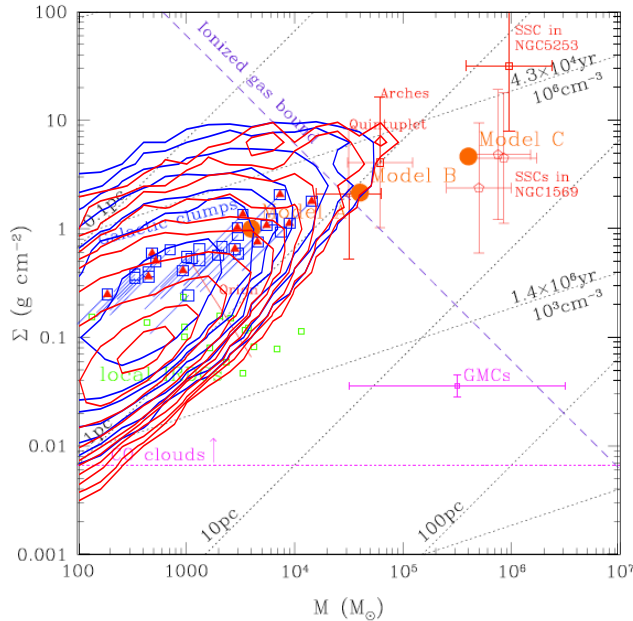


Fig. 11.— Surface density vs. mass diagram from *Tan* (2005), overplotting the nearly 60,000 Hi-GAL detected clumps in the $67^\circ \geq l \geq 19^\circ$, and $-10^\circ \leq l \leq -70^\circ$, for which a distance estimate could be made (*Elia et al.*, 2014). Blue contours are for protostellar clumps, while red contours indicate prestellar clumps (i.e., undetected at $70 \mu\text{m}$). Typical locations of a variety of structures are also indicated. Diagonal contours of constant radius and hydrogen number density or free-fall time scale are shown with dotted lines. The minimum surface density for CO clouds in the local Galactic UV radiation field is shown, as are typical parameters of GMCs. The condition for ionized gas to remain bound is indicated by the dashed line. Locations for a selection of IRDCs (green squares) and dense star-forming clumps (blue squares) are reported (see *Tan* 2005 for a detailed description). Several massive clusters are also indicated.

and evolution including self-gravity (*Vázquez-Semadeni et al.*, 2007, 2009, 2011; *Heitsch and Hartmann*, 2008; *Banerjee et al.*, 2009) suggest that clouds experience global, hierarchical, and chaotic gravitational contraction, so that no support is really necessary.

The transformation of the diffuse ISM involves multiple stages of collapse and fragmentation. The cores in this scenario constitute the last stage of a mass cascade (*Field et al.*, 2008) from the large, HI supercloud scale, through GMCs, down to clumps and individual protostellar cores (*Clark and Bonnell*, 2005; *Vázquez-Semadeni et al.*, 2007, 2009). Collapse occurs along the smallest dimension first, forming sheets, then filaments, and finally clumps, as is expected for pressure-free structures (*Lin et al.*, 1965). This condition applies to GMCs, because their masses are much larger than their Jeans mass. Clumps and cores in this scenario are parts of dynamic rather than hydrostatic structures.

4.3. Triggered Star Formation

Star formation can be triggered by dynamical processes such as protostellar outflows, FUV-driven bubbles, expansion of HII regions, supernova remnants, superbubbles, etc. (*Elmegreen*, 1998; *Deharveng et al.*, 2010; *Elmegreen*, 2011b). Triggering seems to be associated with a local increase of the star formation rate and efficiency (SFR and SFE). Estimates of the percentage of YSOs formed by triggering in the Milky Way lie between 25 and 50% (*Snider et al.*, 2009; *Deharveng et al.*, 2010; *Thompson et al.*, 2012).

In general, any agent that results in converging flows or compression on sufficiently large scales to overcome internal pressure or turbulent support can create conditions for the onset of gravitational instability. Observations show that the highest SFRs occur in regions of extreme pressure and density encountered in galaxy collisions and mergers. The processes act on different scales ranging from small ($\sim \text{pc}$) scale compression of globules, intermediate scale (~ 1 to 10 pc) triggering by expanding FUV-driven bubbles such as NGC 2023 in Orion and EUV-powered HII regions, to larger scale triggering by expanding superbubbles.

Models of triggered star formation were motivated more than a half-century ago by observations of age sequences in nearby OB associations (*Blaauw*, 1991). For example, the 10–15 My old sub-group Ori OB1 is located in the northwest portion of Orion. A sequence of ever younger groups (the 1c, 1b, and 1d sub-groups, *Brown et al.* 1994) extends toward the southeast part of Orion toward the Orion Nebula, which marks the location of the youngest subgroup.

Spatial segregation of age sequences prompted models of triggered, self-propagating star formation in which young second-generation stars form in the shock-compressed layers produced by D-type ionization fronts propagating into clouds with speeds of a few km s^{-1} (*Elmegreen and Lada*, 1977). If the second generation stars are massive, their own HII regions continue the process, forming third generation stars. However, if the clouds have large internal density variations, the D-type shock could lack the coherence required to collect sufficient mass to allow formation of massive stars.

Triggering can occur through compression of pre-existing clumps and cores by application of an external pressure. For example, because the pressure exerted by ionization tends to be orthogonal to the ionization front, clouds and globules overrun by HII regions can be compressed. In principle, application of any external pressure can lead to collapse. However, if the pressure jump is too large, the momentum transfer to the denser medium being overrun causes it to be disrupted rather than compressed. Triggering is most likely when the shocks associated with the external pressure have speeds below the escape speed of the cloud. In this scenario, second generation stars are expected to be younger than the first generation and to have random velocities with respect to them, because they retain the velocity dispersion of the pre-existing cores.

In the collect and collapse mode (*Elmegreen and Lada*,

1977), expanding bubbles sweep up dense shells of gas from the surrounding medium. As such shells accumulate and decelerate, they can become subject to local gravitational instability and collapse resulting in star formation. In this scenario, the younger second generation stars are expected to be moving away from the older generation with a speed of 1 to 10 km s⁻¹. If the medium is relatively uniform, second-generation stars formed earlier from the decelerating shell should have larger velocities and so be located farther from the original stars than those formed later, resulting in an inverted age sequence.

Triggering is an attractive theoretical idea, but the association of YSOs with bubble rims does not necessarily imply that their formation was triggered. The observed morphologies and age sequences could have arisen from spontaneous star formation without the action of the adjacent bubble. The propagation velocities of ionization fronts and shocks decrease and stall when they encounter dense gas. Thus, even for spontaneous, untriggered star formation, bubbles produced by adjacent star formation will run up against other cores and clumps, giving the impression of triggering.

Proof of triggering in the Galactic context requires precise measurements of stellar age and proper motion. Chronometry needs to constrain stellar ages with a time resolution better than the age separation; evidence for age differences using near-IR high-resolution spectroscopy (Martins *et al.*, 2010) are still not conclusive. Proper motions with a precision of a few km s⁻¹ are needed to differentiate pre-existing star formation from triggered star formation. For the nearby star forming complexes, the GAIA mission should soon produce the required proper motion data

4.3.1. Recent observational results

Figure 1 shows young stars and star clusters at the periphery of the giant HII regions in the W3, W4, and W5 complex. The rims of these giant HII regions are surrounded by dense cores, pillars, and hundred of YSOs identified by Spitzer. In the largest and oldest portion of this complex, it has been shown that the formation of these objects was triggered by the expansion of the 3 to 5 My old W5 (Koenig *et al.*, 2008a,b; Koenig and Allen, 2011; Deharveng *et al.*, 2012). For the highest column density, most massive and luminous young clumps found by Herschel in W3, Rivera-Ingraham *et al.* (2013) suggest an active/dynamic “convergent constructive feedback” scenario to account for the formation of a cluster with decreasing age and increasing system/source mass toward the innermost regions and creation of an environment suitable for the formation of a Trapezium-like system.

The Spitzer satellite has revealed many thousands of bubble-shaped ionized regions in the Galaxy. The Milky Way Project (Simpson *et al.*, 2012), combined with other surveys such as the Red MSX Source (RMS, Urquhart *et al.* 2008), led to a statistical study of massive star formation associated with infrared bubbles (Kendrew *et al.*,

2012). About 67%±3% of the Massive Young Stellar Objects (MYSOs) and (ultra-)compact HII regions in the RMS survey are associated with bubbles and 22%±2% of massive young stars might have formed as a result of feedback from expanding HII regions (see also Thompson *et al.* 2012). A similar result was obtained previously by Deharveng *et al.* (2010) using Spitzer-GLIMPSE, Spitzer-MIPSGAL, and ATLASGAL surveys, indicating that about 25% of the bubbles might have triggered the formation of massive objects.

Alexander *et al.* (2013) and Kerton *et al.* (2013) combined Herschel images with HI and radio continuum data to probe bubbles and MYSOs at their periphery. Spectral energy distributions of YSOs derived from Herschel combined with the spatial distribution of sources shows age gradients away from the bubble center in regions such as the Rosette (Schneider *et al.*, 2010b) and N49 (Zavagno *et al.*, 2010).

Hi-GAL has also been used to assess the role of triggering. Hi-GAL sources observed at the edges of HII regions were examined. To determine if these sources and the HII regions are physically associated, we used velocity information from different kinematical surveys (including the MALT90 survey, Foster *et al.* 2011), as well as pointed observations. In particular, we have produced velocity maps toward 300 HII regions (mosaicing the individual MALT90 fields for large regions). Preliminary results show that the velocity fields observed around HII regions using molecular line data agree well with the velocities obtained for the ionized gas from optical and radio recombination line surveys, implying that much of the molecular gas with embedded sources is associated physically with the ionized regions. However, especially in the inner Galaxy other molecular components are observed with different velocities along the line of sight, and our images show that young sources are also observed toward these components. These sources seen in projection near ionized regions might not be physically associated with them and so their formation would have nothing to do with the ionized region and its evolution. Cross-correlation with Hi-GAL distance information will help in sorting out these critical cases (Zavagno *et al.*, 2014).

4.3.2. Recent theoretical developments

Numerical models of the ionization of molecular clouds (Mellema *et al.*, 2006; Arthur *et al.*, 2011; Tremblin *et al.*, 2012a,b) show that compression and photo-erosion produce pillars, elephant trunks, globules, and shells of swept-up, shock-compressed dense gas that can form stars. Radiation-hydrodynamical simulations show the formation of pillars from the curvature fluctuations resulting from turbulence in the dense shell. Ionization of the lower density gas behind the dense pillar heads produces cometary globules (Haworth and Harries, 2012; Haworth *et al.*, 2013). These models predict distinctive velocity fields that can be compared to observations. Haworth *et al.* (2013) developed

molecular line diagnostics of triggered star formation using synthetic observations. *Walch et al. (2013)* use SPH simulations to explore the effects of O stars on a molecular cloud, finding that the structure of swept-up molecular gas can be either shell-like or dominated by pillars and globules, depending on the fractal dimension of the cloud.

5. Star formation thresholds and rates

5.1. Star formation thresholds

5.1.1. Observational studies of local clouds

Is there a column density threshold for star formation in local molecular clouds? Does the SFR increase with density or column density? *Onishi et al. (1998)* mapped the Taurus molecular cloud in $C^{18}O$ and established that prestellar cores (or class 0 protostars) were found only in regions with H_2 column densities greater than $N(H_2) \sim 8 \times 10^{21} \text{ cm}^{-2}$, corresponding to a visual extinction $A_V \sim 8.5$. On the other hand, *Hatchell et al. (2005)* found that in the Perseus cloud the number of cores is a steeply increasing function of the $C^{18}O$ integrated intensity (and, therefore, column density). However, $C^{18}O$ is photo-dissociated at low column densities, becomes optically thick at high column densities, and is depleted in the coldest, densest regions. Thus, dust is a better tracer of the column density. *Johnstone et al. (2004)* mapped the Ophiuchus cloud at $850 \mu\text{m}$ and report that dense cores and Class-0 protostars were found only in regions with $A_V > 7$, indicating an extinction threshold for the formation of dense cores. *Heiderman et al. (2010)* re-examined this issue using a sample of YSOs drawn from the Spitzer c2d survey (*Evans et al., 2009*) and found a steep dependence of the SFR on the surface density, finding a column density threshold $\sim 130 M_\odot \text{ pc}^{-2}$ (cf., Fig. 12), corresponding to $A_V \sim 8.5$. *Lada et al. (2010)* found that the number of YSOs is uncorrelated with the total mass of a cloud, but correlates with the mass above a K-band extinction of 0.8 magnitudes (corresponding to $A_V \sim 7.3$), again consistent with a column density threshold.

Gutermuth et al. (2011) found a steep dependence of the star formation rate on the column density, $\Sigma_{\text{SFR}} \propto \Sigma_{\text{gas}}^2$, rather than a threshold and *Burkert and Hartmann (2013)* also argued that the data are more consistent with a steep, continuous increase of the SFR surface density with gas column density. In a first analysis of the initial Hi-GAL clump sample (*Elia et al., 2014*), *Molinari et al. (2014b)* find good agreement with existing SFR laws (see Fig. 12), but no clear evidence for a sharp column density threshold. Clumps that are considered “prestellar” based on the absence of $70\mu\text{m}$ counterpart and which *Molinari et al. (2014b)* do not use to estimate the SFR, have surface densities that are similar to the “protostellar” clumps (the red-line histogram in Fig. 12). They likely represent clumps that are on the verge of forming stars.

These studies demonstrate that there is a strong dependence of the SFR on column density, but whether/how the SFR continues to increase above some threshold remains

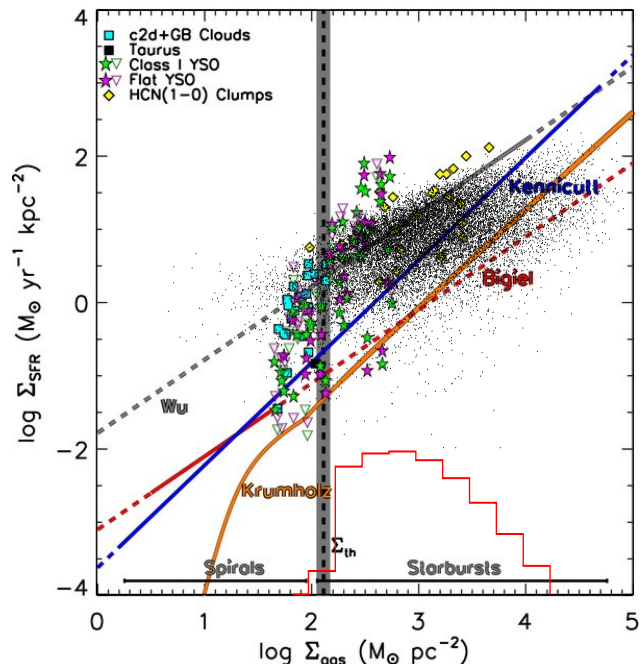


Fig. 12.— Surface density of the SFR vs. mass surface density after *Heiderman et al. (2010)*, including data from many studies thereby referenced. For comparison, the small black dots represent values derived for individual Hi-GAL clumps (*Elia et al., 2014*) classified as protostellar based on the presence of $70 \mu\text{m}$ emission. Because no SFR estimate is available for Hi-GAL prestellar clumps, their distribution in clump surface density is represented by the red line histogram. The ranges of gas surface density for spiral and circumnuclear starburst galaxies in the *Kennicutt (1998)* sample are denoted by the grey horizontal lines. The grey shaded vertical band denotes the threshold surface density Σ_{th} of $129 \pm 14 M_\odot \text{ pc}^{-2}$ (see text). Several $\Sigma_{\text{SFR}} \propto \Sigma_{\text{gas}}$ prescriptions are shown, and we reference to *Heiderman et al. (2010)* for more details.

uncertain.

Is there a threshold column density for the appearance of clumps and cores on filaments? A threshold of $A_V \sim 8$ is reported for the appearance of bound cores on filaments in the Aquila region by *André et al. (2010)* (see André et al., this volume). In the more distant large filamentary complex in the outer Galaxy studied by *Schisano et al. (2014)* no threshold is apparent. In particular, Figure 7 shows a wide range of mass line densities M_{line} for filaments with bound clumps (according to Larson’s criteria as applied by *Elia et al. 2013*). However, the M_{line} distribution for filaments without clumps (green-line histogram) is offset to lower values.

5.1.2. Theoretical models

Two classes of model can explain column density thresholds. In the first, the column density directly affects the likelihood of star formation: star formation is strongly sup-

pressed in gas with a column density below the threshold value. One plausible mechanism is photoelectric heating of the low extinction gas by the interstellar radiation field (ISRF). In turbulent clouds, the complex cloud structure enables radiation to penetrate deeply into the clouds, and the transition from warm, unshielded gas to cooler, shielded gas occurs only when the line-of-sight extinction exceeds $A_V \sim 8$. *Clark and Glover (2013)* show that such a model naturally explains the correlation between the mass of gas with $A_K > 0.8$ and the SFR found by *Lada et al. (2010)*. In their simulations gas with a line-of-sight extinction $A_K > 0.8$ is heated only by cosmic rays, resulting in temperatures lower than in the low-extinction regions that are heated and partially ionized by the ISRF. Therefore, the Jeans mass in the high extinction regions is considerably lower, making gravitational collapse and star formation more likely.

The second class of models is based on a dependence on the volume density, n_{th} , and minimum size, L_{min} . Only regions with column densities exceeding $n_{th}L_{min}$ can form stars. The existence of a volume density threshold is motivated by observations that show that a strong correlation exists between the amount of dense gas and the SFR (see, e.g., *Kennicutt and Evans, 2012*, and references therein). However, simple analytical models based on this correlation tend to predict a continuous dependence of the SFR on the gas density, albeit perhaps steep, rather than the existence of a threshold density (*Krumholz et al., 2012; Burkert and Hartmann, 2013*).

5.2. Star Formation Rates

5.2.1. Observations

The RMS survey has provided statistically significant determinations of the time scales and luminosity functions of massive YSOs and UCHII regions (*Mottram et al., 2011; Davies et al., 2011*). Both the radio-quiet MYSO phase, which could correspond to the swollen, cool, rapidly accreting phase predicted by *Hosokawa et al. (2010)*, and the UCHII-region phase have time scales of one to a few times 10^5 years, depending on the luminosity. The luminosity functions of the two phases are different, with UCHII regions detected up to luminosities of $\sim 10^6 L_\odot$ but no MYSOs above $10^5 L_\odot$, which could be due to rapid evolution of the latter because the MYSO lifetimes become comparable to the Kelvin-Helmholtz time scale, as predicted in the evolutionary models of *Molinari et al. (2008)*. *Davies et al. (2011)* found that luminosity functions and spatial distributions are consistent with accelerating accretion rates as the MYSO grows in mass (predicted by turbulent core and competitive accretion models). Their results rule out models with constant or decreasing accretion rates, implying a global average Galactic SFR of $1.5\text{--}2 M_\odot \text{ yr}^{-1}$. For comparison, the free-fall estimate of the SFR obtained by dividing the total molecular mass in the Galaxy by the free-fall time at the mean density of the molecular gas, is a few $\times 10^2 M_\odot \text{ yr}^{-1}$. Thus, star formation on average in the Galaxy is highly inefficient, with only $\sim 1\%$ of the molec-

ular gas mass being converted to stars in a free-fall time. Equivalently, the depletion time scale of the molecular gas is ~ 1 Gy in the Milky Way, similar to values inferred for nearby galaxies (see, e.g., *Leroy et al., 2013*).

5.2.2. Theory

Models produced in recent years to explain the observed inefficiency of star formation can be grouped into two broad classes (see also the chapters by *Dobbs et al.* and *Padoan et al.* in this volume): “cloud-support” models, in which the SFR is regulated by turbulence that globally maintains the cloud in quasi-equilibrium conditions while inducing local compressions that cause a small fraction of cloud’s mass to collapse per global free-fall time; and “cloud-collapse” models, in which the clouds are assumed to be undergoing collapse on all scales, with small-scale collapses occurring earlier than larger-scale ones, and with an increasing SFR, until the clouds are eventually destroyed by stellar feedback before much of their mass is turned into stars.

A common assumption in all models is that the clouds are internally turbulent and isothermal and therefore characterized by a lognormal density PDF (*Vázquez-Semadeni, 1994; Padoan et al., 1997; Passot and Vázquez-Semadeni, 1998*). The densest regions in the cloud have shorter free-fall times and therefore collapse earlier if they occur in connected regions with more than one Jeans mass. Fluctuations with sufficiently high density will collapse on much shorter time scales than the whole cloud, producing the “instantaneous” SFR within the cloud. The models differ in the way they choose the threshold densities defining the instantaneously-collapsing material, in the time scale associated with this instantaneous SF, and in the global physical conditions in the cloud.

In the cloud-support models (*Krumholz and McKee, 2005; Hennebelle and Chabrier, 2011; Padoan and Nordlund, 2011*), the clouds are in a stationary state and no time dependence is considered. It is interesting to calculate the fraction of the total mass that is converted into stars over a cloud’s free-fall time, ϵ_{ff} (this has been called the “star formation rate per free-fall time” by *Krumholz and McKee 2005*, although by definition it is an *efficiency* achieved on the free-fall time scale). To determine ϵ_{ff} , the cloud is assumed to be in virial equilibrium and to satisfy the Larson linewidth-size relationship. The various models then differ in their choice of the characteristic densities and associated time scales.

Krumholz and McKee (2005) assume that the time scale is close to the global cloud free-fall time, and that the density is that whose corresponding thermal Jeans length equals the sonic scale of the turbulence. The resulting Jeans masses are ~ 0.1 to $2 M_\odot$ (for $T = 10\text{--}40$ K), comparable to the mean masses of stars. Note, however, that numerical simulations of isothermal, driven turbulence do not confirm the existence of the required hypothetical clumps that are simultaneously subsonic and super-Jeans (*Vázquez-Semadeni et al., 2008*). *Padoan and Nordlund (2011)* in-

stead assume that the relevant time scale is the free-fall time at the threshold density, and that this density is determined by the magnetic shock jump conditions and the magnetic critical mass for collapse. Finally, *Hennebelle and Chabrier* (2011) assume that the density threshold is such that its *turbulent* (i.e., including the turbulent velocity dispersion as a source of pressure) Jeans length is a specified fraction of the system scale, implying that this threshold is scale-dependent because the turbulent motions in general exhibit a scale dependence described by the turbulent energy spectrum. For the time scale, these authors assume that each density above the threshold collapses on its own free-fall time, a feature they term “multi-free-fall.” They also propose multi-free-fall versions of the *Krumholz and McKee* (2005) and *Padoan and Nordlund* (2011) theories.

In general, the turbulent-support models predict the dependence of ϵ_{ff} on various parameters of the clouds, such as the rms turbulent Mach number \mathcal{M} , the virial parameter α (the ratio of kinetic to gravitational energy in the cloud), and, when magnetic fields are considered, the magnetic β parameter (the ratio of thermal to magnetic pressure). *Federrath and Klessen* (2012) show that the multi-free-fall versions of these models all predict $\epsilon_{\text{ff}} \sim 1\text{--}10\%$, in qualitative agreement with observations.

On the other hand, cloud-collapse models (*Zamora-Avilés et al.*, 2012) assume that the clouds are in free-fall and therefore that both their density and instantaneous star-forming mass fraction are time dependent. These authors calibrate the threshold density for instantaneous SF by comparing to the simulations of *Vázquez-Semadeni et al.* (2010), take the associated time scale as the free-fall time at the threshold density, and assume that the evolution ends when the cloud is finally destroyed. They find that the SFR is generally increasing and compares favorably with the evolutionary times scales for GMCs in the LMC (*Kawamura et al.*, 2009) and the stellar-age histograms of *Palla and Stahler* (2000, 2002). Moreover, *Zamora-Avilés and Vázquez-Semadeni* (2013) also find that the time-averaged SFR as a function of cloud mass compares favorably with the relation found by *Gao and Solomon* (2004).

An intermediate class of models has been presented by *Krumholz et al.* (2006) and *Goldbaum et al.* (2011). They compute the time-dependent virial balance of the clouds assuming spherical symmetry and that the expansion of HII regions drives supporting turbulence in the clouds, whereas winds produced by massive stars escape the clouds. Their models predict that the clouds undergo an oscillatory stage that is short for low-mass clouds and longer (several free-fall times) for more massive clouds.

A crucial difference between the various models is the assumed effect of stellar feedback on the clouds, which ranges from simply driving turbulence to entirely evaporating them. Recent numerical simulations have addressed this issue, finding that while on short time scales (~ 1 My) stellar ionizing feedback indeed drives turbulence into the clouds (*Gritschneider et al.*, 2009; *Walch et al.*, 2012), the final effect on time scales ~ 10 My is the destruction of the

star-forming site for clouds up to $10^5 M_{\odot}$ (*Dale et al.*, 2012, 2013; *Colín et al.*, 2013).

5.3. Cloud Disruption

The low SFE in gravitationally unbound molecular clouds is a consequence of their dissolution in a crossing time, $L/\sigma \sim 3$ to 10 My for 10 – 30 pc clouds obeying Larson’s laws. Bound clouds require energy inputs to be disrupted and dissociated. Feedback from forming stars is the most likely agent. For instance, feedback from low-mass ($M < \text{few } M_{\odot}$) stars is dominated by their outflows (*Li and Nakamura* 2006; *Wang et al.* 2010; *Nakamura and Li* 2011). Although stars of all masses generate such flows during formation, in more massive stars other mechanisms inject greater amounts of energy after accretion stops. Intermediate mass YSOs ($2 < M < 8 M_{\odot}$) produce copious non-ionizing radiation that heats adjacent cloud surfaces to temperatures of 10^2 to over 6×10^3 K, raising the sound speed to 1–6 km s $^{-1}$ and dramatically increasing pressure in the heated layer. The resulting gas expansion can drive shocks into surrounding gas, accelerating it. Chaotic cloud structure results in chaotic motions. Late B and A stars are thus an important source of heating, motion, and turbulence generation through the action of their photon-dominated regions. High mass ($M > 8 M_{\odot}$) stars ionize their environments, creating 10^4 K HII regions whose pressure accelerates surrounding gas.

The growth of HII regions and their feedback on the structure of molecular clouds has been studied by many different groups (see, e.g., *Franco et al.*, 1994; *Matzner*, 2002; *Walch et al.*, 2012). Small molecular clouds are efficiently disrupted by ionizing radiation on short time scales, but the largest Galactic GMCs have escape velocities that are significantly higher than the sound speed of photoionized gas, and are therefore not disrupted (see, e.g., *Krumholz et al.*, 2006; *Dale et al.*, 2012)

In massive GMCs radiation pressure from absorbed or scattered photons could be important (*Murray et al.*, 2010). For single scattering or absorption, the momentum transferred to surrounding gas is $\dot{P} \sim L\tau/c \sim 1.3 \times 10^{29} \tau L_6$ g cm s $^{-2}$ where τ is the optical depth and L_6 is the total embedded bolometric luminosity in units of $10^6 L_{\odot}$. Because stars generally form in the densest parts of clouds, this momentum transfer contributes to gas dispersal. The effectiveness of this form of feedback depends on both how much radiation is produced by the stars and what fraction of this radiation is trapped by the cloud (*Krumholz and Thompson*, 2013). Radiation can leak out through cavities in highly structured clouds, lowering its effectiveness as a feedback mechanism; this is the case for most Galactic GMCs.

During their accretion phase, all stars produce powerful MHD-powered bipolar outflows whose momentum injection rate is 10 to 100 times L/c . When massive stars form, their outflows are likely to clear channels through which radiation can leak out of the parent clump, decreasing the feedback from radiation pressure. Models of the effects

of radiation pressure on star-forming clouds show that in low-mass clouds radiative trapping is small and that photoionization is more important than radiation pressure for destroying clouds (Agertz *et al.*, 2013). Radiative trapping could be larger in more massive clouds, although Krumholz and Thompson (2013) argue that Rayleigh-Taylor instability of pressure-driven gas dramatically reduces its effective optical depth (but see Kuiper *et al.* 2013).

Feedback from outflows, FUV, ionizing radiation, and radiation pressure produce comparable momentum injection rates. In turn, these are similar to momentum dissipation rates for typical parameters. This points to a dynamic balance between dissipation and injection. Furthermore, the low SFE in typical GMCs suggests that once the SFE reaches 2–20%, feedback wins and disrupts the cloud. Failure of feedback could lead to high SFE and formation of bound clusters (Bressert *et al.*, 2012).

OB stars that eventually explode as type II supernovae have lifetimes of 3–30 My, longer than GMC lifetimes. Stellar winds, radiation pressure, and the supernovae generated have powerful feedback on clouds, even those at dozens or hundreds of pc from the explosion site as observations of the local superbubbles show. Supernovae probably play the dominant role in driving turbulence on large scales in the ISM (Mac Low and Klessen, 2004).

5.4. Global mapping of thresholds and SFRs

An assessment of the available estimates of the present day SFR in the Milky Way was carried out by Chomiuk and Povich (2011) using a common IMF and stellar models applied to measured free-free emission rates and mid-IR YSO counts. Their median result is $1.9 \pm 0.4 M_{\odot} \text{ yr}^{-1}$. The GLIMPSE and MIPS GAL surveys (Robitaille *et al.*, 2008) result in a modeled SFR $\sim 0.68 - 1.45 M_{\odot} \text{ yr}^{-1}$ (Robitaille and Whitney, 2010); the main uncertainty arises from contamination by AGB stars. Using the classic method of measuring the Lyman continuum luminosity from HII regions free-free radio continuum Murray and Rahman (2010) use the WMAP data to find SFR = $1.3 \pm 0.2 M_{\odot} \text{ yr}^{-1}$, for a Salpeter IMF, and values between 0.9 and $2.2 M_{\odot} \text{ yr}^{-1}$ for a range of IMF slopes. This may be a lower bound since it not clear that the analysis of WMAP free-free emission properly accounts for Lyman continuum lost from the Galaxy that leaks out of chimneys to illuminate the Lockman layer.

Kennicutt and Evans (2012) present a review connecting the Galactic star formation with extragalactic systems. Evans *et al.* (2009) and Lada *et al.* (2010) found that for a given surface density in nearby molecular clouds the extragalactic Schmidt-Kennicutt relationship underestimates the SFR, because studies of the SFR in Galactic GMCs tend to ignore the surface density from extensive, non-star-forming gas; when this is included, the Galactic SFRs fit the extragalactic relationship. An example of this is shown in Figure 12, where Heiderman *et al.* (2010) plot local clouds and Galactic clumps onto the extragalactic star formation relationship. The figure shows an order of magnitude range in

SFR at any given gas surface density. For individual proto-stellar clumps cataloged by Elia *et al.* (2014) using Hi-GAL data, we can derive the SFR and mass per unit area. These are overplotted as small black dots in Figure 12.

Herschel provides a wealth of data on the formation rate of massive stars in different Galactic environments. For example, in four square degrees at longitudes $l = 30^{\circ}$ (near the Scutum arm tangent) and at $l = 59^{\circ}$ (Russeil *et al.*, 2011; Veneziani *et al.*, 2013) Hi-GAL found average rates of $\sim 10^{-3}$ and $\sim 10^{-4} M_{\odot} \text{ yr}^{-1}$, respectively. In the rich massive star-forming region G305 Faimali *et al.* (2012) found rates of $0.01 - 0.02 M_{\odot} \text{ yr}^{-1}$. In the $l = 217 - 224^{\circ}$ region situated in the outer Galaxy at Galactocentric distances greater than 10kpc Elia *et al.* (2013) found a value of $\sim 5 \times 10^{-4} M_{\odot} \text{ yr}^{-1}$. Veneziani *et al.* (2014) analyze the star formation content at the tips of the Galactic Bar using the same method as in their 2013’s paper, but also incorporating a statistical correction to predicted luminosities to account for the fact that these clumps host protoclusters rather than single massive forming stars; they find values $\sim 1.5 \times 10^{-3} M_{\odot} \text{ yr}^{-1} \text{ kpc}^{-2}$, at both sides of the Bar. Globally combining all of the massive objects in the preliminary Hi-GAL catalog, limited to the $+67^{\circ} \geq l \geq -70^{\circ}$ range and *excluding* the inner ~ 25 degrees of the Central Molecular Zone, Molinari *et al.* (2014b) find a total SFR $\sim 0.2 M_{\odot} \text{ yr}^{-1}$, that can be considered a lower limit especially because only a fraction, although significant, of the Galaxy is considered.

The conversion efficiency of molecular gas into dense potentially star-forming clumps and into stellar luminosity has been examined by Eden *et al.* (2012) and Moore *et al.* (2012) as a function of position, both in and out of spiral arms. There is little or no increase in SFE associated with the Scutum-tangent region and the near end of the Galactic bar, which includes the W43 complex. Investigation of the Galactic distribution of the ~ 1650 embedded, young massive objects in the RMS survey, one third of which are above the completeness limit of $\sim 2 \times 10^4 L_{\odot}$ (Urquhart *et al.*, 2013a), shows that the distribution of massive star formation in the Milky Way is correlated with a model of four spiral arms. The increase in SFR density in spiral arms is due to the pile-up of clumps, rather than to a higher specific rate of conversion of clumps into stars (a higher SFE). That the source and luminosity surface densities of RMS sources are correlated with the surface density of the molecular gas, suggests that the massive star-formation rate per unit molecular mass is approximately constant across the Galaxy. The total luminosity of the embedded massive-star population is found to be $\sim 0.8 \times 10^8 L_{\odot}$, 30% of which is associated with the ten most active star forming complexes.

Given the enormous reservoir of dense H_2 in the CMZ, a high SFR might be expected there. Local relationships (Lada *et al.*, 2012; Krumholz, 2012) extrapolated to Galactic Center conditions predict $0.18 - 0.74 M_{\odot} \text{ yr}^{-1}$ (based on extinction) or $0.14 - 0.4 M_{\odot} \text{ yr}^{-1}$ (based on volume density). Surprisingly, however, Yusef-Zadeh *et al.* (2009) and Immer *et al.* (2012) found $0.08 - 0.14 M_{\odot} \text{ yr}^{-1}$, also

consistent with the Schmidt-Kennicutt relationship. Using WMAP free-free emission as a tracer of star formation within 500 pc of the Galactic Center (about 1 kpc^{-2}), Longmore et al. (2013b) found even lower values, 3.6×10^{-3} to $1.6 \times 10^{-2} M_{\odot} \text{ yr}^{-1}$, again in disagreement with predictions.

6. Conclusions

The avalanche of new infrared to radio continuum and spectroscopic imaging of the Galactic Plane is a goldmine that we are just starting to exploit, and yet more are desirable. Current quadrant-scale CO spectroscopic surveys of the 3rd and 4th quadrants only deliver super-arcminute resolution. Sub-arcmin CO surveys are required; this effort is indeed starting to be assembled (see Table 1) but more is needed. Additional high spatial resolution surveys in molecular tracers like NH_3 and other high-density tracers are also needed. Considerable potential also resides in post-Herschel unbiased arc-second resolution continuum surveys in the far-IR and submm, as well as in the radio where sensitivities of current unbiased surveys are still not adequate for detailed Galactic studies. These will be within reach of future facilities like SPICA, CCAT, MILLIMETRON and the SKA pathfinders, while ALMA and JWST will be able to concentrate on selected samples of star-forming complexes. Large-scale sub-arcminute resolution polarization surveys in the far-IR and submm are badly needed to ascertain the role of magnetic fields throughout the cloud-filament-clump-core evolutionary sequence.

In our opinion, however, the real challenge and opportunities lie in an “industrial revolution” of the science analysis methodologies in Galactic astronomy. Current approaches are largely inadequate to execute a timely and effective scientific exploitation of complete Galactic Plane surveys covering several hundreds of square degrees. Progress is needed in tools for pattern recognition and extraction of clumps, filaments, bubbles, and sheets in highly variable background conditions, for robust construction of SEDs, for evolutionary classification of compact clumps and cores, and for 3D vector modeling of Galactic rotation incorporating streaming motions, to name a few. Toward building a Galactic plane knowledge base, we envision these technical developments integrated within a framework of data mining, machine learning, and interactive 3D visualization, so as to transfuse the astronomer’s know-how into a set of automated and supervised tools with decision-making capabilities.

REFERENCES

Abdo A. A. et al. (2010) *Astrophys. J.*, 710, 133.
 Agertz O. et al. (2013) *Astrophys. J.*, 770, 25.
 Aguirre J. E. et al. (2011) *Astrophys. J. Suppl.*, 192, 4.
 Alexander M. et al. (2013) *Astrophys. J.*, 770, 1.
 Allen R. J. et al. (2004) *Astrophys. J.*, 608, 314.
 Allen R. J. et al. (2012) *Astron. J.*, 143, 97.
 Alves J. et al. (2007) *Astron. Astrophys.*, 462, L17.
 André P. et al. (2010) *Astron. Astrophys.*, 518, L102.

Arthur S. J. et al. (2011) *Mon. Not. R. Astron. Soc.*, 414, 1747.
 Arzoumanian D. et al. (2011) *Astron. Astrophys.*, 529, L6.
 Audit E. and Hennebelle P. (2005) *Astron. Astrophys.*, 433, 1.
 Ballesteros-Paredes J. et al. (1999) *Astrophys. J.*, 527, 285.
 Ballesteros-Paredes J. et al. (2007) *Protostars and Planets V*, pp. 63–80.
 Ballesteros-Paredes J. et al. (2011) *Mon. Not. R. Astron. Soc.*, 411, 65.
 Bally J. (2010) *Nature*, 466, 928.
 Bally J. et al. (1987a) *Astrophys. J. Lett.*, 312, L45.
 Bally J. et al. (1987b) *Astrophys. J. Suppl.*, 65, 13.
 Bally J. et al. (2010) *Astrophys. J.*, 721, 137.
 Banerjee R. et al. (2009) *Mon. Not. R. Astron. Soc.*, 398, 1082.
 Barnard E. E. (1907) *Astrophys. J.*, 25, 218.
 Barnes P. J. et al. (2011) *Astrophys. J. Suppl.*, 196, 12.
 Barnes P. J. et al. (2013) *Astrophys. J.*, in prep.
 Battersby C. et al. (2011) *Astron. Astrophys.*, 535, A128.
 Beltrán M. T. et al. (2006) *Astron. Astrophys.*, 447, 221.
 Benjamin R. A. and GLIMPSE360 Team (2013) AAS Meeting #222, #303.03.
 Benjamin R. A. et al. (2003) *PASP*, 115, 953.
 Beuther H. et al. (2007) *Protostars and Planets V*, pp. 165–180.
 Binney J. et al. (1991) *Mon. Not. R. Astron. Soc.*, 252, 210.
 Blaauw A. (1991) in: *NATO ASIC Proc. 342: The Physics of Star Formation and Early Stellar Evolution*, (edited by C. J. Lada and N. D. Kylafis), p. 125.
 Bressert E. et al. (2012) *Astrophys. J. Lett.*, 758, L28.
 Brown A. G. A. et al. (1994) *Astron. Astrophys.*, 289, 101.
 Brunthaler A. et al. (2011) *Astronomische Nachrichten*, 332, 461.
 Burkert A. and Hartmann L. (2013) *Astrophys. J.*, 773, 48.
 Burton M. G. et al. (2013) *PASA*, 30, 44.
 Butler M. J. and Tan J. C. (2012) *Astrophys. J.*, 754, 5.
 Carey S. J. et al. (2000) *Astrophys. J. Lett.*, 543, L157.
 Carey S. J. et al. (2009) *PASP*, 121, 76.
 Chapman N. L. et al. (2011) *Astrophys. J.*, 741, 21.
 Chomiuk L. and Povich M. S. (2011) *Astron. J.*, 142, 197.
 Clark P. and Bonnell I. (2005) *Mon. Not. R. Astron. Soc.*, 361, 2.
 Clark P. C. and Glover S. C. O. (2013) *ArXiv e-prints*, 1306.5714.
 Clark P. C. et al. (2012) *Mon. Not. R. Astron. Soc.*, 424, 2599.
 Colín P. et al. (2013) *Mon. Not. R. Astron. Soc.*, 435, 1701.
 Combes F. (1991) *Annu. Rev. Astron. Astrophys.*, 29, 195.
 Contreras Y. et al. (2013) *Astron. Astrophys.*, 549, A45.
 Dahmen G. et al. (1998) *Astron. Astrophys.*, 331, 959.
 Dale J. E. et al. (2012) *Mon. Not. R. Astron. Soc.*, 424, 377.
 Dale J. E. et al. (2013) *Mon. Not. R. Astron. Soc.*, 430, 234.
 Dame T. M. et al. (1986) *Astrophys. J.*, 305, 892.
 Dame T. M. et al. (1987) *Astrophys. J.*, 322, 706.
 Dame T. M. et al. (2001) *Astrophys. J.*, 547, 792.
 Davies B. et al. (2011) *Mon. Not. R. Astron. Soc.*, 416, 972.
 de Zeeuw P. T. et al. (1999) *Astron. J.*, 117, 354.
 Deharveng L. et al. (2010) *Astron. Astrophys.*, 523, 6.
 Deharveng L. et al. (2012) *Astron. Astrophys.*, 546, 74.
 di Francesco J. et al. (2007) *Protostars and Planets V*, pp. 17–32.
 Dobbs C. L. et al. (2008) *Mon. Not. R. Astron. Soc.*, 389, 1097.
 Dobbs C. L. et al. (2012) *Mon. Not. R. Astron. Soc.*, 425, 2157.
 Eden D. J. et al. (2012) *Mon. Not. R. Astron. Soc.*, 422, 3178.
 Egan M. P. et al. (1998) *Astrophys. J. Lett.*, 494, L199.
 Ehlervová S. and Palouš J. (2013) *Astron. Astrophys.*, 550, A23.
 Elia D. et al. (2013) *Astrophys. J.*, 772, 45.
 Elia D. et al. (2014) *Astron. Astrophys.*, in preparation.
 Ellsworth-Bowers T. P. et al. (2013) *Astrophys. J.*, 770, 39.
 Elmegreen B. G. (1994) *Astrophys. J.*, 433, 39.

- Elmegreen B. G. (1998) *ASP Conference Series*, 148, 150.
- Elmegreen B. G. (2011a) *Astrophys. J.*, 737, 10.
- Elmegreen B. G. (2011b) *Triggered Star Formation*, vol. 51, EAS Publications Series.
- Elmegreen B. G. and Elmegreen D. M. (1987) *Astrophys. J.*, 320, 182.
- Elmegreen B. G. and Lada C. J. (1977) *Astrophys. J.*, 214, 725.
- Evans II N. J. et al. (2009) *Astrophys. J. Suppl.*, 181, 321.
- Faimali A. et al. (2012) *Mon. Not. R. Astron. Soc.*, 426, 402.
- Fallscheer C. et al. (2013) *Astrophys. J.*, 773, 102.
- Federrath C. and Klessen R. S. (2012) *Astrophys. J.*, 761, 156.
- Ferrière K. et al. (2007) *Astron. Astrophys.*, 467, 611.
- Field G. B. (1965) *Astrophys. J.*, 142, 531.
- Field G. B. et al. (2008) *Mon. Not. R. Astron. Soc.*, 385, 181.
- Fischera J. and Martin P. G. (2012a) *Astron. Astrophys.*, 547, A86.
- Fischera J. and Martin P. G. (2012b) *Astron. Astrophys.*, 542, A77.
- Foster J. B. et al. (2011) *Astrophys. J. Suppl.*, 197, 25.
- Foster J. B. et al. (2013) *PASA*, 30, 38.
- Franco J. et al. (1994) *Astrophys. J.*, 436, 795.
- Gao Y. and Solomon P. M. (2004) *Astrophys. J.*, 606, 271.
- Gibson S. J. et al. (2000) *Astrophys. J.*, 540, 851.
- Ginsburg A. et al. (2012) *Astrophys. J. Lett.*, 758, L29.
- Ginsburg A. et al. (2013) *Astrophys. J. Suppl.*, 208, 14.
- Glover S. C. O. and Mac Low M.-M. (2007) *Astrophys. J. Suppl.*, 169, 239.
- Glover S. C. O. and Mac Low M.-M. (2011) *Mon. Not. R. Astron. Soc.*, 412, 337.
- Goldbaum N. J. et al. (2011) *Astrophys. J.*, 738, 101.
- Goldsmith P. F. et al. (2008) *Astrophys. J.*, 680, 428.
- Gómez G. C. and Vázquez-Semadeni E. (2013) *Astrophys. J.*, 428, 186.
- Green J. A. et al. (2009) *Mon. Not. R. Astron. Soc.*, 392, 783.
- Grenier I. A. et al. (2005) *Science*, 307, 1292.
- Gritschneider M. et al. (2009) *Astrophys. J. Lett.*, 694, L26.
- Gutermuth R. A. et al. (2011) *Astrophys. J.*, 739, 84.
- Hacar A. and Tafalla M. (2011) *Astron. Astrophys.*, 533, A34.
- Hartmann D. and Burton W. B. (1997) *Atlas of Galactic Neutral Hydrogen*.
- Hartmann L. et al. (2001) *Astrophys. J.*, 562, 852.
- Hatchell J. et al. (2005) *Astron. Astrophys.*, 440, 151.
- Haworth T. J. and Harries T. J. (2012) *Mon. Not. R. Astron. Soc.*, 420, 562.
- Haworth T. J. et al. (2013) *Mon. Not. R. Astron. Soc.*, 431, 3470.
- Heiderman A. et al. (2010) *Astrophys. J.*, 723, 1019.
- Heiner J. S. and Vázquez-Semadeni E. (2013) *Mon. Not. R. Astron. Soc.*, 429, 3584.
- Heiner J. S. et al. (2009) *Astrophys. J.*, 700, 545.
- Heitsch F. and Hartmann L. (2008) *Astrophys. J.*, 689, 290.
- Heitsch F. et al. (2005) *Astrophys. J. Lett.*, 633, L113.
- Heitsch F. et al. (2008) *Astrophys. J.*, 674, 316.
- Hennebelle P. and Chabrier G. (2011) *Astrophys. J. Lett.*, 743, L29.
- Hennebelle P. and Pérault M. (1999) *Astron. Astrophys.*, 351, 309.
- Heyer M. et al. (2009) *Astrophys. J.*, 699, 1092.
- Heyer M. H. et al. (1998) *Astrophys. J. Suppl.*, 115, 241.
- Hill T. et al. (2011) *Astron. Astrophys.*, 533, 94.
- Hoare M. G. et al. (2012) *PASP*, 124, 939.
- Hosokawa T. et al. (2010) *Astrophys. J.*, 721, 478.
- Huettemeister S. et al. (1998) *Astron. Astrophys.*, 334, 646.
- Ikeda N. et al. (2007) *Astrophys. J.*, 665, 1194.
- Immer K. et al. (2012) *Astron. Astrophys.*, 548, A120.
- Ishihara D. et al. (2010) *Astron. Astrophys.*, 514, A1.
- Jackson J. M. et al. (2006) *Astrophys. J. Suppl.*, 163, 145.
- Johnstone D. and Bally J. (1999) *Astrophys. J. Lett.*, 510, L49.
- Johnstone D. and Bally J. (2006) *Astrophys. J.*, 653, 383.
- Johnstone D. et al. (2004) *Astrophys. J. Lett.*, 611, L45.
- Jones P. A. et al. (2012) *Mon. Not. R. Astron. Soc.*, 419, 2961.
- Jones P. A. et al. (2013) *Mon. Not. R. Astron. Soc.*, 433, 221.
- Kalberla P. M. W. and Kerp J. (2009) *Annu. Rev. Astron. Astrophys.*, 47, 27.
- Kauffmann J. and Pillai T. (2010) *Astrophys. J. Lett.*, 723, L7.
- Kawamura A. et al. (2009) *Astrophys. J. Suppl.*, 184, 1, 1.
- Kendrew S. et al. (2012) *Astrophys. J.*, 755, 71.
- Kennicutt Jr. R. C. (1998) *Astrophys. J.*, 498, 541.
- Kennicutt Jr. R. C. and Evans II N. J. (2012) *Annu. Rev. Astron. Astrophys.*, 50, 531.
- Kerton C. R. et al. (2013) *Astron. J.*, 145, 78.
- Kirk H. et al. (2013a) *Astrophys. J.*, 766, 115.
- Kirk J. M. et al. (2013b) *Mon. Not. R. Astron. Soc.*, 432, 1424.
- Koenig X. P. and Allen L. E. (2011) *Astrophys. J.*, 726, 18.
- Koenig X. P. et al. (2008a) *Astrophys. J.*, 688, 1142.
- Koenig X. P. et al. (2008b) *Astrophys. J. Lett.*, 687, L37.
- Koo B. et al. (1992) *Astrophys. J.*, 390, 108.
- Koyama H. and Inutsuka S.-I. (2000) *Astrophys. J.*, 532, 980.
- Koyama H. and Inutsuka S.-i. (2002) *Astrophys. J. Lett.*, 564, L97.
- Kruijssen J. M. D. et al. (2013) *ArXiv e-prints*, 1303.6286.
- Krumholz M. R. (2012) *Astrophys. J.*, 759, 9.
- Krumholz M. R. and McKee C. F. (2005) *Astrophys. J.*, 630, 250.
- Krumholz M. R. and McKee C. F. (2008) *Nature*, 451, 1082.
- Krumholz M. R. and Thompson T. A. (2013) *Mon. Not. R. Astron. Soc.*, 434, 2329.
- Krumholz M. R. et al. (2006) *Astrophys. J.*, 653, 361.
- Krumholz M. R. et al. (2012) *Astrophys. J.*, 745, 69.
- Kuiper R. et al. (2013) in: *The Labyrinth of Star Formation*, Springer.
- Kuntz K. D. and Danly L. (1996) *Astrophys. J.*, 457, 703.
- Lada C. J. et al. (2007) *Protostars and Planets V*, pp. 3–15.
- Lada C. J. et al. (2010) *Astrophys. J.*, 724, 687.
- Lada C. J. et al. (2012) *Astrophys. J.*, 745, 190.
- Larson R. B. (1981) *Mon. Not. R. Astron. Soc.*, 194, 809.
- Larson R. B. (1985) *Mon. Not. R. Astron. Soc.*, 214, 379.
- Lee M.-Y. et al. (2012) *Astrophys. J.*, 748, 75.
- Leroy A. et al. (2013) *Astron. J.*, 146, 19.
- Lesh J. R. (1968) *Astrophys. J. Suppl.*, 17, 371.
- Li Z.-Y. and Nakamura F. (2006) *Astrophys. J. Lett.*, 640, L187.
- Lin C. C. et al. (1965) *Astrophys. J.*, 142, 1431.
- Lindblad P. O. et al. (1973) *Astron. Astrophys.*, 24, 309.
- Longmore S. N. et al. (2012) *Astrophys. J.*, 746, 117.
- Longmore S. N. et al. (2013a) *Mon. Not. R. Astron. Soc.*, 433, L15.
- Longmore S. N. et al. (2013b) *Mon. Not. R. Astron. Soc.*, 429, 987.
- Mac Low M.-M. and Klessen R. S. (2004) *Reviews of Modern Physics*, 76, 125.
- Martin C. L. et al. (2004) *Astrophys. J. Suppl.*, 150, 239.
- Martins F. et al. (2010) *Astron. Astrophys.*, 510, 32.
- Matzner C. D. (2002) *Astrophys. J.*, 566, 302.
- McClure-Griffiths N. M. et al. (2001) *Astrophys. J.*, 551, 394.
- McCray R. and Kafatos M. (1987) *Astrophys. J.*, 317, 190.
- McKee C. F. and Ostriker E. C. (2007) *Annu. Rev. Astron. Astrophys.*, 45, 565.
- Mellema G. et al. (2006) *Astrophys. J.*, 647, 397.
- Mizuno A. and Fukui Y. (2004) in: *Milky Way Surveys: The Structure and Evolution of our Galaxy*, vol. ASP Conference Series 317, p. 59.
- Molinari S. et al. (2008) *Astron. Astrophys.*, 481, 345.
- Molinari S. et al. (2010a) *Astron. Astrophys.*, 518, L100.

- Molinari S. et al. (2010b) *PASP*, 122, 314.
- Molinari S. et al. (2011) *Astrophys. J. Lett.*, 735, L33.
- Molinari S. et al. (2014a) *Astron. Astrophys.*, in preparation.
- Molinari S. et al. (2014b) *Astrophys. J.*, in preparation.
- Moore T. J. T. et al. (2012) *Mon. Not. R. Astron. Soc.*, 426, 701.
- Morris M. and Serabyn E. (1996) *Annu. Rev. Astron. Astrophys.*, 34, 645.
- Motte F. et al. (1998) *Astron. Astrophys.*, 336, 150.
- Mottram J. C. et al. (2011) *Astrophys. J. Lett.*, 730, L33.
- Murray N. and Rahman M. (2010) *Astrophys. J.*, 709, 424.
- Murray N. et al. (2010) *Astrophys. J.*, 709, 191.
- Myers P. C. (2009) *Astrophys. J.*, 700, 1609.
- Nakamura F. and Li Z.-Y. (2011) *Astrophys. J.*, 740, 36.
- Narayanan G. et al. (2008) *Astrophys. J. Suppl.*, 177, 341.
- Olmi L. et al. (2013) *Astron. Astrophys.*, 551, 111.
- Onishi T. et al. (1998) *Astrophys. J.*, 502, 296.
- Padoan P. and Nordlund Å. (2002) *Astrophys. J.*, 576, 870.
- Padoan P. and Nordlund Å. (2011) *Astrophys. J.*, 730, 40.
- Padoan P. et al. (1997) *Mon. Not. R. Astron. Soc.*, 288, 145.
- Padoan P. et al. (2001) in: *ASP Conference Series*, vol. 243, p. 279.
- Palla F. and Stahler S. W. (2000) *Astrophys. J.*, 540, 255.
- Palla F. and Stahler S. W. (2002) *Astrophys. J.*, 581, 1194.
- Palmeirim P. et al. (2013) *Astron. Astrophys.*, 550, A38.
- Passot T. and Vázquez-Semadeni E. (1998) *Phys. Rev. E*, 58, 4501.
- Peretto N. and Fuller G. A. (2009) *Astron. Astrophys.*, 505, 405.
- Peretto N. et al. (2013) *Astron. Astrophys.*, 555, 112.
- Perrot C. A. and Grenier I. A. (2003) *Astron. Astrophys.*, 404, 519.
- Pezzuto S. et al. (2014) *Astron. Astrophys.*, in prep.
- Pillai T. et al. (2006) *Astron. Astrophys.*, 450, 569.
- Pineda J. L. et al. (2013) *Astron. Astrophys.*, 554, A103.
- Planck Collaboration et al. (2011) *Astron. Astrophys.*, 536, A19.
- Planck Collaboration et al. (2013a) *ArXiv e-prints*, 1303.5062.
- Planck Collaboration et al. (2013b) *ArXiv e-prints*, 1303.5073.
- Planck Collaboration et al. (2013c) *Astron. Astrophys.*, 554, A139.
- Plume R. et al. (1992) *Astrophys. J. Suppl.*, 78, 505.
- Plume R. et al. (1997) *Astrophys. J.*, 476, 730.
- Polychroni D. et al. (2013) *Astrophys. J. Lett.*, 777, 33.
- Pon A. et al. (2012) *Astrophys. J.*, 756, 145.
- Price S. D. et al. (2001) *Astron. J.*, 121, 2819.
- Pringle J. E. et al. (2001) *Mon. Not. R. Astron. Soc.*, 327, 663.
- Purcell C. R. et al. (2012) *Mon. Not. R. Astron. Soc.*, 426, 1972.
- Reid M. A. and Wilson C. D. (2005) *Astrophys. J.*, 625, 891.
- Rivera-Ingraham A. et al. (2013) *Astrophys. J.*, 766, 85.
- Robitaille T. P. and Whitney B. A. (2010) *Astrophys. J. Lett.*, 710, L11.
- Robitaille T. P. et al. (2008) *Astron. J.*, 136, 2413.
- Roman-Duval J. et al. (2010) *Astrophys. J.*, 723, 492.
- Rosolowsky E. (2005) *PASP*, 117, 1403.
- Rosolowsky E. et al. (2010) *Astrophys. J. Suppl.*, 188, 123.
- Russeil D. et al. (2011) *Astron. Astrophys.*, 526, 151.
- Schisano E. et al. (2014) *Astrophys. J.*, submitted.
- Schneider N. et al. (2010a) *Astron. Astrophys.*, 520, 49.
- Schneider N. et al. (2010b) *Astron. Astrophys.*, 518, L83.
- Schneider N. et al. (2012) *Astron. Astrophys.*, 540, L11.
- Schneider S. and Elmegreen B. G. (1979) *Astrophys. J. Suppl.*, 41, 87.
- Schuller F. et al. (2009) *Astron. Astrophys.*, 504, 415.
- Shirley Y. et al. (2003) *Astrophys. J. Suppl.*, 149, 375.
- Simon R. et al. (2006) *Astrophys. J.*, 653, 1325.
- Simpson R. J. et al. (2012) *Mon. Not. R. Astron. Soc.*, 424, 2442.
- Snider K. D. et al. (2009) *Astrophys. J.*, 700, 506.
- Sofue Y. and Handa T. (1984) *Nature*, 310, 568.
- Stark A. A. et al. (1992) *Astrophys. J. Suppl.*, 79, 77.
- Stil J. et al. (2006) *Astron. J.*, 132, 1158.
- Su M. et al. (2010) *Astrophys. J.*, 724, 1044.
- Tackenberg J. et al. (2012) *Astron. Astrophys.*, 540, 113.
- Tan J. C. (2005) in: *Cores to Clusters: Star Formation with Next Generation Telescopes*, p. 87.
- Thompson M. A. et al. (2012) *Mon. Not. R. Astron. Soc.*, 421, 408.
- Toalá J. A. et al. (2012) *Astrophys. J.*, 744, 190.
- Toomre A. (1964) *Astrophys. J.*, 139, 1217.
- Tremblin P. et al. (2012a) *Astron. Astrophys.*, 538, A31.
- Tremblin P. et al. (2012b) *Astron. Astrophys.*, 546, 33.
- Urquhart J. S. et al. (2008) in: *ASP Conference Series*, vol. 387, (edited by A. S. of the Pacific), p. 381.
- Urquhart J. S. et al. (2013a) *Mon. Not. R. Astron. Soc.*, 431, 1752.
- Urquhart J. S. et al. (2013b) *Mon. Not. R. Astron. Soc.*, 435, 400.
- Vázquez-Semadeni E. (1994) *Astrophys. J.*, 423, 681.
- Vázquez-Semadeni E. et al. (2000) *Astrophys. J.*, 540, 271.
- Vázquez-Semadeni E. et al. (2006) *Astrophys. J.*, 643, 245.
- Vázquez-Semadeni E. et al. (2007) *Astrophys. J.*, 657, 870.
- Vázquez-Semadeni E. et al. (2008) *Mon. Not. R. Astron. Soc.*, 390, 769.
- Vázquez-Semadeni E. et al. (2009) *Astrophys. J.*, 707, 1023.
- Vázquez-Semadeni E. et al. (2010) *Astrophys. J.*, 715, 1302.
- Vázquez-Semadeni E. et al. (2011) *Mon. Not. R. Astron. Soc.*, 414, 2511.
- Veneziani M. et al. (2013) *Astron. Astrophys.*, 549, 130.
- Veneziani M. et al. (2014) *Astron. Astrophys.*, submitted.
- Wada K. et al. (2002) *Astrophys. J.*, 577, 197.
- Walch S. et al. (2013) *Mon. Not. R. Astron. Soc.*, 435, 917.
- Walch S. K. et al. (2012) *Mon. Not. R. Astron. Soc.*, 427, 625.
- Walsh A. J. et al. (2011) *Mon. Not. R. Astron. Soc.*, 416, 1764.
- Wang P. et al. (2010) *Astrophys. J.*, 709, 27.
- Ward-Thompson D. et al. (2007) *Protostars and Planets V*, pp. 33–46.
- Wienen M. et al. (2012) *Astron. Astrophys.*, 544, 146.
- Wilcock L. A. et al. (2012) *Mon. Not. R. Astron. Soc.*, 424, 716.
- Wolfire M. G. et al. (2010) *Astrophys. J.*, 716, 1191.
- Wright E. L. et al. (2010) *Astron. J.*, 140, 1868.
- Xu Y. et al. (2013) *Astrophys. J.*, 769, 15.
- Yusef-Zadeh F. et al. (2009) *Astrophys. J.*, 702, 178.
- Zamora-Avilés M. and Vázquez-Semadeni E. (2013) *ArXiv e-prints*, 1308.4918.
- Zamora-Avilés M. et al. (2012) *Astrophys. J.*, 751, 77.
- Zavagno A. et al. (2010) *Astron. Astrophys.*, 518, L101.
- Zavagno A. et al. (2014) *Astron. Astrophys.*, in prep.